University of Texas Rio Grande Valley

ScholarWorks @ UTRGV

Mechanical Engineering Faculty Publications and Presentations

College of Engineering and Computer Science

2-8-2018

Direct Numerical Simulation of Transverse Ripples: 2. Self-Similarity, Bedform Coarsening, and Effect of Neighboring Structures

Nadim Zgheib

J. J. Fedele

D. C. J. D. Hoyal

M. M. Perillo

S. Balachandar

Follow this and additional works at: https://scholarworks.utrgv.edu/me_fac

Part of the Mechanical Engineering Commons

AGU PUBLICATIONS

JGR

Journal of Geophysical Research: Earth Surface

RESEARCH ARTICLE
10.1002/2017JF004399

This article is a companion to Zgheib et al. (2018) https://doi.org/10.1002/2017JF004398.

Key Points:
- Isolated ripples maintain a self-similar shape and bed shear stress profiles
- Bedform-bedform interactions can significantly modify bedform celerity
- Spectra of bed height variation suggest a Reynolds number dependence

Supporting Information:
- Supporting Information S1
- Movie S1
- Movie S2
- Movie S3
- Movie S4
- Movie S5
- Movie S6
- Movie S7
- Movie S8
- Movie S9
- Movie S10
- Movie S11

Correspondence to:
N. Zgheib,
nadim.zgheib@lau.edu.lb

Citation:
Zgheib, N., Fedele, J. J., Hoyal, D. C. J. D., Perillo, M. M., & Balachandar, S. (2018). Direct numerical simulation of transverse ripples: 2. Self-similarity, bedform coarsening, and effect of neighboring structures. *Journal of Geophysical Research: Earth Surface*, *123*, 478–500. https://doi.org/10.1002/2017JF004399

Received 15 JUN 2017
Accepted 29 JAN 2018
Accepted article online 8 FEB 2018
Published online 9 MAR 2018

©2018. American Geophysical Union. All Rights Reserved.

Direct Numerical Simulation of Transverse Ripples: 2. Self-Similarity, Bedform Coarsening, and Effect of Neighboring Structures

N. Zgheib[1,2], J. J. Fedele[3], D. C. J. D. Hoyal[3], M. M. Perillo[3], and S. Balachandar[1]

[1]Department of Mechanical and Aerospace Engineering, University of Florida, Gainesville, FL, USA, [2]School of Engineering, Lebanese American University, Byblos, Lebanon, [3]ExxonMobil Upstream Research Company, Houston, TX, USA

Abstract Coupled bed-flow direct numerical simulations investigating the early stages of pattern formation and bedform (ripple) interactions were examined in a previous paper (Part 1), making use of the resolved flow field. In this paper (Part 2), we compare our results to published experimental data and provide an extensive quantitative analysis of the bed using spectral analysis and two-point correlations. The effect of the mobile rippled bed on the flow structure and turbulence is investigated locally (at specific streamwise locations) and over the entire computational domain. We show that developing ripples attain a self-similar profile in both the shape and the corresponding bed shear stress. We demonstrate the importance of neighboring structures, especially upstream neighbors, on bedform dynamics in terms of the growth, decay, and speed of ripples. Finally, we examine the defect-free interactions in the later stages of bed evolution, which primarily lead to wave coarsening.

1. Introduction

In the companion paper (Zgheib et al., 2018), hereafter referred to as Paper 1, we examined the early stages of bed evolution and the reproducibility of the various stages of bed development, starting from a flattened bed. Using the near-bed flow field, we provided evidence on the role of locally intense vortical structures in initiating quasi-streamwise sediment streaks that evolve into incipient crestlines. Additionally, we investigated in detail the fluid mechanical origins of a number of defect-related bedform interactions and showed that for flow-aligned interactions, the underlying mechanism is very similar and that interactions are labeled differently depending on the geometry of interacting structures and the outcome of the interaction.

Substantial research over the past two decades has yielded a wealth of information on the spatial structure of mature ripples as well as their time evolution and interaction (Ashley, 1990; Best, 1992; Best & Kostaschuk, 2002; Charru & Mouilleron-Arnould, 2002; Charru et al., 2013; Coco & Murray, 2007; Gyr & Schmid, 1997; Howard, 2007; Kocurek et al., 2010; Ouriemi et al., 2009a, 2009b; Ribberink & Al-Salem, 1994; Swanson et al., 2016; Werner, 1995, 1999, 2003). In this paper, we focus on the later stages of bed evolution in which ripples are found to attain a nearly self-similar, asymmetrical, triangular-like shape with a gentle slope on the stoss side and a steeper slope on the lee side corresponding to the angle of repose. At any instance during bed evolution, the size, and thus the speed, of bedforms may be different, which result in bedform interactions as smaller/faster ripples catch up to downstream larger/slower neighbors. Consequently, during the later stages of bed evolution, when the ripples span the entire width of the domain, these interactions primarily lead to wave coarsening. The coarsening process is fascinating and perhaps counterintuitively driven by the smaller upstream ripples starving their larger downstream neighbors (Coleman & Melville, 1994). Additionally, we find that the coarsening process could be responsible in part for the relatively large scatter observed in experimental as well as numerical data pertaining to ripple speed and growth rate.

Similarly, there is a great body of literature on the mean flow and turbulence statistics over ripples and dunes. Significant emphasis in the past has been on investigating the simplified case of turbulent flow over fixed bedforms (Balachandar et al., 2003; Bennett & Best, 1995; Coleman et al., 2006; Grigoriadis et al., 2009; Kadota & Nezu, 1999; Maddux et al., 2003; McLean et al., 1994; Nelson & Smith, 1989; Omidyeganeh & Piomelli, 2013; Venditti & Bennett, 2000; Yue et al., 2005; Zedler & Street, 2001). The resulting turbulence is statistically stationary, and this assumption is justified on the basis that the evolution of the bed is on a

21699011, 2018, 3, Downloaded from https://agupubs.onlinelibrary.wiley.com/doi/10.1002/2017JF004399 by The University Of Texas Rio Grande Valley, Wiley Online Library on [17/02/2023]. See the Terms and Conditions (https://onlinelibrary.wiley.com/terms-and-conditions) on Wiley Online Library for rules of use; OA articles are governed by the applicable Creative Commons License

21699011, 2018, 3, Downloaded from https://agupubs.onlinelibrary.wiley.com/doi/10.1002/2017JF004399 by The University Of Texas Rio Grande Valley, Wiley Online Library on [17/02/2023]. See the Terms and Conditions (https://onlinelibrary.wiley.com/terms-and-conditions) on Wiley Online Library for rules of use; OA articles are governed by the applicable Creative Commons License

time scale much longer than that of the turbulent flow. Furthermore, these investigations typically consider a fully developed ripple structure that has reached an equilibrium state. These studies focus on the main flow features such as the space- and time-averaged flow field, flow separation on the lee side, and size of recirculation region, as well as turbulent fluctuations at various streamwise positions. On the other hand, experimental or numerical studies showing the turbulence structure under mobile bed conditions (Coleman & Nikora, 2011; Hanmaiahgari & Balachandar, 2016; Schindler & Robert, 2005) have been limited but have yielded valuable information.

One of the methods for quantifying the structure and topology of bedforms is through the spectra of bed height variation (Hino, 1968; Jain & Kennedy, 1974; Nikora et al., 1997). In experiments, because of the difficulty in measuring bed elevation over the entire planform at the same time during a run, it is often the spectra of the equilibrium bedforms in the final stage of bedform evolution that is reported (Perillo et al., 2014). Alternatively, the instantaneous two-point correlation of bed height variation in numerical simulations may be used to assess certain features including the stage of development of bedforms and the temporal rate of wave coarsening (Kidanemariam & Uhlmann, 2014, 2017). Similarly, spatiotemporal correlations of bedforms are used to relate the speed to the size of the bedforms.

An interesting aspect of fully formed ripple and other bedform patterns is their self-similar nature (e.g., Andrle, 1996; Coleman et al., 2006; Franklin & Charru, 2009; Pelletier, 2013). In the context of barchan dunes, Franklin and Charru (2009) found a self-similar shape for isolated dunes in both eolian and subaqueous environments suggesting that their shape is independent of the transport mechanism. On the other hand, by conducting experiments on fixed two-dimensional dunes, Coleman et al. (2006) found that the flow in the near-bed region, specifically in the boundary layer, exhibits a self-similar profile. They argued that this near-bed, self-similar flow is central to the understanding of the feedback loop between the flow and underlying bed.

The purpose of this paper is to examine the self-similar state of fully developed ripples and establish their statistical properties. Cross-sectional shape of the ripple, ripple height to wavelength ratio, and ripple speed as a function ripple height will be examined and compared with available experimental data. The self-similarity of the resulting flow field in terms of shear stress and recirculation region downstream of the ripple will also be examined. Direct numerical simulation (DNS) results enable us to characterize the near-wall turbulence statistics as modified by the mobile bedforms and compare results against those established for fixed bedforms. The remainder of this paper is organized as follows. An examination of ripple properties from bedform spectra, Fourier expansions, two-point correlations, and turbulence and mean flow statistics is presented in section 2 followed by a quantitative analysis of ripple self-similarity in section 3. The process of wave coarsening and the inevitable scatter it introduces to wave speed and growth rate is discussed in section 4. Discussion and conclusions are presented in sections 5 and 6, respectively.

2. Spectra, Wave Properties, and Two-Point Correlation

2.1. Bedform Spectra

Before we begin our discussion on bedform spectra, we would like to note that Tables 1 and 2 from Paper 1, which define many of the variables and provide details about the simulations, are included in this part of the manuscript for completeness. The simulations considered in this section are for cases S1 through S6 of Table 2, those evolving from an initially flat surface. The sediment bed height variation initially grows at an exponential rate (e.g., Fourrière et al., 2010; Jerolmack & Mohrig, 2005; Kidanemariam & Uhlmann, 2017) before approaching a plateau beyond the equilibrium stage of development. In Figure 1 we show the temporal evolution of the maximum ($h_{\max}$) and rms (h_{rms}) values of the sediment bed height variation. Here $h_{\max}$ and h_{rms} are defined as follows:

$$h_{\max}(t) = \max_{x,y}\left[h(x,y,t)\right] \;\; ; \;\; h_{\mathrm{rms}}(t) = \sqrt{\frac{1}{L_x L_y}\int_0^{L_y}\int_0^{L_x} h^2 \mathrm{d}x\mathrm{d}y}, \tag{1}$$

where $h(x, y, t)$ is the bed height with reference to the initial flat bed, which remains as the mean bed height at all later time. The streamwise, spanwise, and vertical directions are denoted by x, y, and z, respectively. We

Table 1
Symbols, Notation, and Nomenclature Definition

Variable/notation	Symbol	Mathematical expression/definition
	Scaling variables	
Mean flow depth (length scale)	H_f^*	—
Mean shear velocity (velocity scale)	U_τ^*	—
Time scale	T^*	H_f^*/U_τ^*
	Flow-related variables	
3-D velocity field	$\boldsymbol{u}$	
Perturbation pressure	p	
Numerical domain size (streamwise × spanwise × vertical)	$L_x \times L_y \times L_z$	—
Numerical resolution	$N_x \times N_y \times N_z$	—
Bulk velocity	U_b	$\frac{1}{L_y H_f}\int_0^{L_y}\int_0^{H_f} u\,dz\,dy$
Fluid density	ρ_f^*	—
Gravitational acceleration	g^*	—
Fluid kinematic viscosity	ν^*	—
Fluid dynamic viscosity	μ^*	—
Particle Reynolds number	Re_p	$\frac{1}{\nu^*}\sqrt{\frac{\rho_p^*-\rho_f^*}{\rho_f^*} g^* d_p^{*3}}$
Shear Reynolds number	Re_τ	$U_\tau^* H_f^*/\nu^*$
	Bed-related variables	
Bed shear stress	τ^*	$\left(\frac{\mu^* U_\tau^*}{H_f^*}\right)\frac{\partial u}{\partial n}$
Shields number	Θ	$\tau^*/\left[\left(\rho_p^*-\rho_f^*\right)g^* d_p^*\right]$
Critical Shields number	Θ_{cr}	$\frac{1}{2}\left[0.22\ \mathrm{Re}_p^{-0.6} + 0.06\ \exp\left(-17.77\ \mathrm{Re}_p^{-0.6}\right)\right]$
Volumetric flux of sediment per unit width[a]	q	$\left(\mathrm{Re}_p/\mathrm{Re}_\tau\right) c_1 (\Theta-\Theta_{cr})^{c_2}$
Bed volume fraction	φ	1 − porosity
Diffusion coefficient	ϵ	—
Bed elevation (with respect to mean)	h	—
Mean bed height	$\overline{h}$	—
Sediment diameter	d_p^*	—
Sediment density	ρ_p^*	—
	Notation	
Unit vector	$\boldsymbol{e}$	
x, y, z, bed-tangent, bed-normal components of quantity ■	$\{■_x, ■_y, ■_z, ■_t, ■_n\}$	
Time average of quantity ■	$\langle ■ \rangle$	$\frac{1}{T}\int_{t_1}^{t_1+\psi} ■\,dt$
Spanwise average of quantity ■	$\overline{■}$	$\frac{1}{L_y}\int_0^{L_y} ■\,dy$
Stream and span average of quantity ■	$\overline{\overline{■}}$	$\frac{1}{L_x L_y}\int_0^{L_y}\int_0^{L_x} ■\,dx\,dy$

Note. Asterisk denotes dimensional quantity.
[a]Based on the MPM (1948) modified Wong and Parker (2006) model (c1 = 4.93, c2 = 1.6)

remind the reader that all quantities have been nondimensionalized. The velocity scale corresponds to the friction velocity U_τ^* defined in terms of the mean streamwise pressure gradient as $\rho_f^* U_\tau^{*2}/H_f^* = -\nabla^* p^*$, where the length scale H_f^* represents the mean flow depth. Here and in the remainder of the paper, the asterisk denotes a dimensional quantity (similar to Paper 1). While $h_{\max}$ may locally attain values of about 8 to 15% of the mean flow depth, h_{rms} remains bounded to less than 5%. h_{rms} is a simple and common

21699011, 2018, 3, Downloaded from https://agupubs.onlinelibrary.wiley.com/doi/10.1002/2017JF004399 by The University Of Texas Rio Grande Valley, Wiley Online Library on [17/02/2023]. See the Terms and Conditions (https://onlinelibrary.wiley.com/terms-and-conditions) on Wiley Online Library for rules of use; OA articles are governed by the applicable Creative Commons License

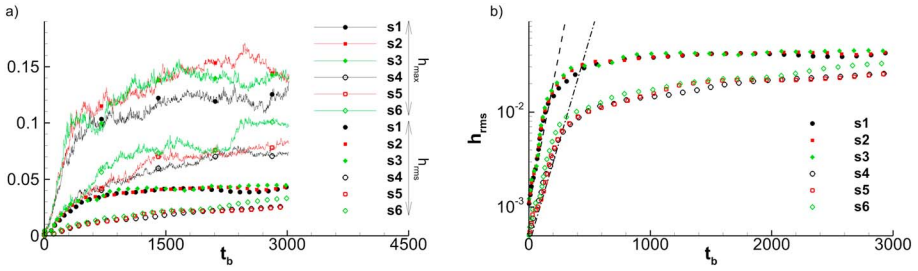

Figure 1. (a) Temporal evolution of the maximum and rms bed height fluctuation. (b) Same as Figure 1a but with linear log scale to show the exponential growth of h_{rms}. The exponential growth is observed in approximately the first 200 bulk time units. The dashed and dash-dotted lines correspond to exponential fits of $h_{rms} = 10^{-3}$ exp $(0.015t_b)$ and $h_{rms} = 4 \times 10^{-4}$ exp $(0.01t_b)$, respectively.

measure of surface roughness and is sometimes referred to as the interface width (e.g., Barabási & Stanley, 1995; Jerolmack & Mohrig, 2005). We observe from Figure 1 a strong dependence on the flow shear velocity. Cases S1 through S3, with the higher U_τ^* value, evolve faster than the lower U_τ^* cases S4 through S6. This observation applies to both h_{max} and h_{rms}. We also observe a weak dependence of h_{max} on the grain size. Simulations with the smaller grain size (cases S3 and S6) grow marginally faster than the corresponding larger grain simulations (cases S1 and S4). However, this dependence is only observed for later times, $t_b \gtrsim 600$ and is not detected for h_{rms}. Here t_b represents nondimensional time in bulk units ($t_b = t^* U_b/H_f$), and $U_b \approx 15.6U_\tau$ is the initial bulk velocity obtained from the span- and depth-averaged flow field.

The initial exponential growth of h_{rms} can be observed in the log linear plot of Figure 1b, and the curve fits follow

$$h_{rms} = 10^{-3} \exp(0.015t_b) \quad \text{and} \quad h_{rms} = 4\times10^{-4} \exp(0.01t_b) \tag{2}$$

for the high and low shear stress cases, respectively. Thus, the rate of increase in bed height variation for the higher shear stress cases is 50% larger than that for the lower shear stress cases. But the initial exponential growth only lasts for about $t_b \approx 150$ and $t_b \approx 250$ for the high and low shear stress cases, respectively. This is the period of formation of initial crestlines and their interaction and merger to form well-defined ripples. We should note that the exponential growth rate of 0.015 for the higher shear stress cases S1 through S3 is closer to the value of 0.014 observed by Kidanemariam and Uhlmann (2017) in comparison to the slower growth rate of 0.01 for the lower shear stress cases. Additionally, we find the duration of the exponential growth of bedforms for cases S1 through S3, which is about 200 bulk units to be very similar to that observed in Kidanemariam and Uhlmann (2017). The better agreement of the higher shear stress cases with the DNS results of Kidanemariam and Uhlmann (2017) is due to the fact that for cases S1 through S3, the ratio $\Theta/\Theta_{cr} \approx 4$ (see Table 2), is closer to the range of values used in Kidanemariam and Uhlmann (2017).

Subsequent evolution of the bed is at a much slower rate. During the initial period of this slower evolution the ripples continue to form and complete their evolution toward their approximate self-similar state. Even after they are fully formed, the ripples continue to interact through the merging and coarsening process. In terms of wall units, toward the end of the simulation, the rms bed height variation reaches about $h_{rms+} = 6.5$ and 8.0 for the high and low shear rate cases, and the corresponding peak ripple heights are about $h_{max+} = 14.5$ and 27, respectively. Thus, the ripples can be expected to substantially alter the nature of wall turbulence. We should note here that the ripple height (if interpreted as a roughness length scale) is in the hydraulically smooth regime (regarding the rms value) and at the lower end of the transitionally rough regime (regarding the maximum amplitude).

One of the methods for quantifying the structure and topology of bedforms is through the spectra of bed height variation. In experiments, because of the difficulty in measuring bed elevation over the entire planform at the same time during a run, it is often the spectra of the equilibrium bedforms in the final stage of bedform evolution that is reported. Hino (1968), Jain and Kennedy (1974), and Nikora et al. (1997) have reported a -3 power decay for large wave numbers in the spectra of bed

21699011, 2018, 3, Downloaded from https://agupubs.onlinelibrary.wiley.com/doi/10.1002/2017JF004399 by The University Of Texas Rio Grande Valley, Wiley Online Library on [17/02/2023]. See the Terms and Conditions (https://onlinelibrary.wiley.com/terms-and-conditions) on Wiley Online Library for rules of use; OA articles are governed by the applicable Creative Commons License

Table 2
List of Simulations Presented in Paper 1 and Shown Here for Completeness

Simulation number	d_p^* (μm)	ρ_p^* (g/cm^3)	ρ_f^* (g/cm^3)	Re_p	Θ_{cr}	Θ	Θ/Θ_{cr}	Re_τ	U_τ^* (cm/s)	U_b^* (cm/s)	H_f^* (cm)	H_b^* (mm)	$L_x \times L_y \times L_z$	$N_x \times N_y \times N_z$
S1	250	1.57	1.015	9.347	0.029	0.109	3.76	180	1.237	19.32	1.455	0.728	12 × 4 × 1.05	288 × 96 × 301
S2	150	1.57	1.015	4.344	0.046	0.182	4.00	180	1.237	19.32	1.455	0.728	12 × 4 × 1.05	288 × 96 × 301
S3	50	1.57	1.015	0.836	0.122	0.547	4.47	180	1.237	19.32	1.455	0.728	12 × 4 × 1.05	288 × 96 × 301
S4	250	1.57	1.015	9.347	0.029	0.055	1.88	180	0.874	13.65	2.058	1.03	12 × 4 × 1.05	288 × 96 × 301
S5	150	1.57	1.015	4.344	0.046	0.091	2.00	180	0.874	13.65	2.058	1.03	12 × 4 × 1.05	288 × 96 × 301
S6	50	1.57	1.015	0.836	0.122	0.274	2.23	180	0.874	13.65	2.058	1.03	12 × 4 × 1.05	288 × 96 × 301

Note. d_p^*, ρ_p^*, and ρ_f^* are the sediment diameter, sediment density, and fluid density respectively. Re_p is the sediment Reynolds number. Θ_{cr} is the critical Shields number, and Θ is the Shields number imposed by the flow. Re_τ is the shear Reynolds number based on the bed shear velocity U_τ^* and flow depth H_f^*. U_b^* and H_b^* are the bulk velocity and sediment thickness, respectively. L_x, L_y, and L_z represent the computational domain length, width, and height, respectively. N_x, N_y, and N_z correspond to the number of grid points along the streamwise, spanwise, and vertical directions, respectively.

height variation. On the other hand, Kidanemariam and Uhlmann (2017) have reported a spectral power decay between −4.3 and −3.5 for their DNS. The shear Reynolds number for which the −3 power decay was reported was in the range of $5 \times 10^3 < Re_\tau < 10^6$, which is more than an order of magnitude larger than $250 < Re_\tau < 350$ considered by Kidanemariam and Uhlmann (2017). In the present set of simulations for which $Re_\tau = 180$, we observe a decay rate of −3.75 (Figure 2), closer to the range reported by Kidanemariam and Uhlmann (2017). The spectra at four different times for case S2 are shown in Figure 2, and similar decay is observed for the other five cases. The larger spectral decay rate in the present study and in Kidanemariam and Uhlmann (2017) may suggest a Reynolds number dependence.

It can be observed that the spectra show an exponential decay at the very early time of $t_b = 5$. By $t_b = 98$, well-formed crestlines appear contributing to the power law decay rate. The peak in the spectra at $k = 8$ corresponds to the emergence of about eight crestlines that occupy the streamwise extent of the computational domain. As the bed evolves, the spectra move up indicating temporal increase in the rms value of the bed height variation. Furthermore, the peak in the spectra moves from $k = 8$ to lower values indicating the coarsening of ripples. At $t_b = 500$, the peak is located at $k = 4$, and $t_b = 2{,}381$, the peak is located at $k = 3$ indicating the dominance of four and three ripples at these times.

2.2. Turbulence Statistics and Flow Separation

The patterns that form from the bed-flow interactions are not sinusoidal but take a more triangular shape as shown in Part 1 of the manuscript. In the following, we investigate the overall effect of a mobile rippled bed on the flow field. Figure 3 shows the rms velocity fluctuations for the streamwise, spanwise, and vertical components of velocity as well as the Reynolds stress versus distance from the bed for case S2. We consider two stages: (i) a completely flat bed (solid red line) and (ii) a mobile, rippled bed (black dashed and green dash-dotted lines). The first stage is representative of the start of the present simulations and corresponds to the classical pressure-driven open-channel turbulent flow over a smooth wall, whereas the second corresponds to a pressure-driven open-channel turbulent flow over a complex, time-evolving rippled topology. The presence of the ripples contributes to macroscopic (large-scale) roughness induced form drag (Einstein & Barbarossa, 1952; Engelund, 1977; Fedele & García, 2001). As a result, when the bed was completely flat (at $t_b = 0$), the streamwise pressure gradient was entirely balanced by skin friction along the bed. At later times, the pressure gradient is partly balanced by skin friction and partly by form drag. Thus, in the present simulations where the driving mean pressure gradient was held fixed (Re_τ is a constant), the formation of bedforms results in a lowering of the mean shear stress. At the start of the simulation at $t_b = 0$ when the bed is still completely flat, the local streamwise, spanwise, and bed-normal directions (in the frame of reference of the bed) coincide with the x, y, and z directions, respectively. However, as the shear stress is allowed to work and modify the bed, the bed-tangent and bed-normal directions will no longer be necessarily aligned with the horizontal and vertical directions. To that end, we present the data for $t_b > 1{,}000$ in Figure 3 in two coordinate frames. We should note here that this analysis is done in postprocessing with a simple change of coordinate system. The first coordinate frame is aligned with the computational domain such that the streamwise, spanwise, and vertical components of velocity are along the x, y, and z directions, respectively, irrespective of the shape of the bed, whereas in the second coordinate frame, the alignment of these velocity components is with respect to the bed. The former coordinate frame is more appropriate away from the bed, where the direct effect of the ripples on the flow is relatively weak and the streamlines are predominantly aligned with the x direction. On the other hand, the bed-based coordinate frame is more appropriate in the near-bed region where the streamlines are strongly dependent on the shape of the bed. These two coordinate frames are denoted by z_v and z_n for the former and the latter, respectively. Note that in both coordinate frames, the fluid/sediment interface corresponds to $z_v = 0$ and $z_n = 0$ (recall that both coordinate

21699011, 2018, 3, Downloaded from https://agupubs.onlinelibrary.wiley.com/doi/10.1002/2017JF004399 by The University Of Texas Rio Grande Valley, Wiley Online Library on [17/02/2023]. See the Terms and Conditions (https://onlinelibrary.wiley.com/terms-and-conditions) on Wiley Online Library for rules of use; OA articles are governed by the applicable Creative Commons License

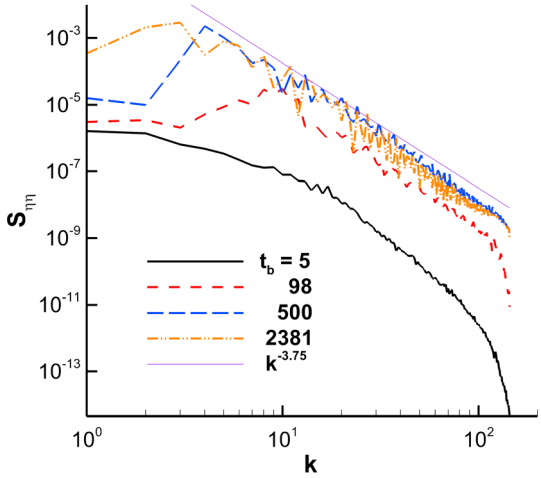

Figure 2. Wave number spectra from S2 at five time instances. For $t_b > 500$, we observe a decay rate of -3.75 (thin solid purple line).

frames extend from the bed outward). The peak Reynolds shear stress for the flat bottom boundary (red curve in frame d) occurs at around 30 wall units above the bed in the buffer region, well above the viscous sublayer. The location of the peak is slightly lower (black dash curve) in the case of the rippled bed, and this is consistent with the reduction in the mean wall shear stress, as part of the pressure gradient is balanced by form drag.

We observe the streamwise and spanwise velocity fluctuations (u_{xrms} and u_{yrms}) to be weakly dependent on the choice of coordinate frame. Alternatively, u_{zrms} (frame c) and the Reynolds stress (frame d) exhibit a significant difference between the two coordinate frames showing the importance of choosing the correct description of bed-normal distance in the near-bed and far field regions. For example, the Reynolds stress in Figure 3d, when computed in the computational coordinate frame, initially attains a negative value near the bed, before changing signs and attaining positive values at around $z \approx 0.08$. However, when the bed-normal coordinate frame is employed, the results are qualitatively and quantitatively different. We do not observe qualitative differences in the profile of the velocity fluctuations or the Reynolds stress due to the presence of the ripples. We do, however, observe the velocity fluctuations to increase near the bed. This near-bed rise in the rms velocity values comes at the expense of the mean flow, which is constrained by the presence of the ripples and consequently reduced over time as seen in Figure 4. It should be noted that in the bed-normal coordinate system, the plot of u_{zrms} remains a constant with increasing z_n and this is due to the fact that away from the bed, a component of the streamwise velocity fluctuation appears as the bed-normal component. Thus, the optimal coordinate appears to be one that is normal to the bed in the near-bed region and turns to the vertical direction sufficiently far away.

It is important to understand how the mean velocity profile is affected by the presence of bedforms. Figure 4 shows the vertical z profile of the stream- and span-averaged x component of the flow at different time instances for case S2. We take the position of the bed into consideration by using the z_v coordinate. Recall that $z_v = z - h(x, y, t)$ represents the vertical distance from the bed. The red solid line corresponds to the

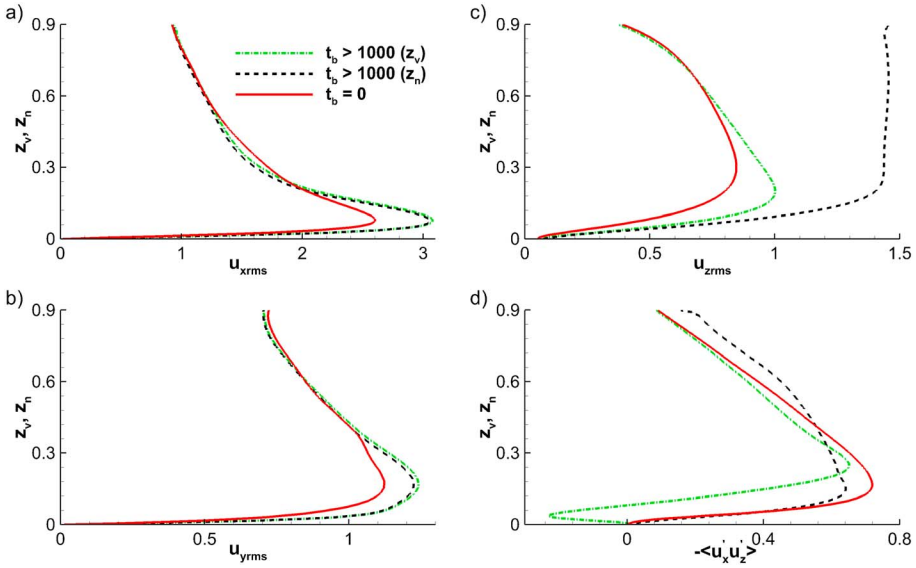

Figure 3. rms velocity fluctuations over the entire computational domain versus distance from the bed (z_v, z_n) for the (a) streamwise, (b) spanwise, and (c) and vertical components of velocity for case S2 at the start of the simulation (solid red line) and beyond t_b = 1,000 (black dashed and green dash-dotted lines). (d) Same as other frames but for Reynolds stress $- < u_x' u_z' >$.

21699011, 2018, 3, Downloaded from https://agupubs.onlinelibrary.wiley.com/doi/10.1002/2017JF004399 by The University Of Texas Rio Grande Valley, Wiley Online Library on [17/02/2023]. See the Terms and Conditions (https://onlinelibrary.wiley.com/terms-and-conditions) on Wiley Online Library for rules of use; OA articles are governed by the applicable Creative Commons License

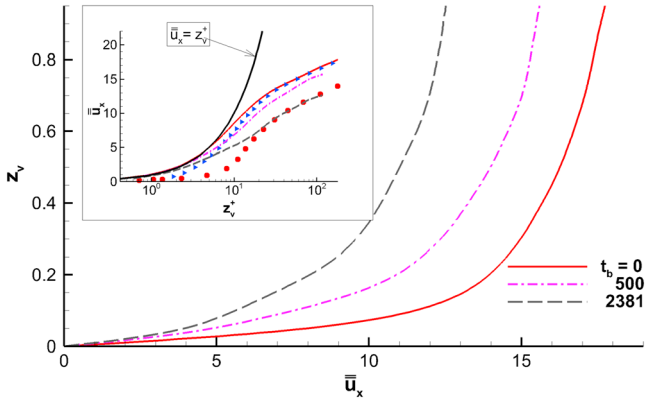

Figure 4. Stream- and span-averaged x component of velocity versus vertical distance from the bed z_v at different instances for case S2. (Inset) same as main figure but for wall units z_v^+ on a log linear plot. The symbols correspond to velocity profile from an actual rough wall simulation (Chan-Braun et al., 2011). Note that the axes in the main figure and inset are inverted.

velocity profile at the start of the simulation when the bed is completely flat. Two other time instances are considered, namely, t_b = 500 (purple dash-dotted line) and t_b = 2,381 (black dashed line). The inset of Figure 4 shows a log linear plot of $\overline{\overline{u}}_\tau$ in wall units ($z_v^+ = z_v^* \overline{\overline{u}}_\tau^* / \nu^*$) for the same time instances (note that the axes are flipped between the main figure and the inset). The thick solid black line corresponds to $\overline{\overline{u}}_\tau = z_v^+$ and conforms to the velocity profile in the viscous sublayer. Note that z_v^+ and z^+ are identical at the start of the simulation as the bed is completely flat. The blue triangular and red circular symbols in the inset correspond to results from a rough wall, open-channel flow, fully resolved DNS (Chan-Braun et al., 2011). The geometrically rough wall in the simulations of Chan-Braun et al. (2011) consisted of a layer of spheres in a square arrangement. Two arrangements were considered. The first case (blue triangles in Figure 4) had small spheres whose diameter is equivalent to 10.7 wall units, whereas for the second case (red circles) the spheres were larger with an equivalent diameter of 49.3 wall units. The Reynolds number of the flow, based on bulk velocity, was around $Re_b \approx 2900$, which is comparable to the bulk Reynolds number of our simulations ($Re_b \approx 2{,}800$). As expected, we find that as the bedforms grow in amplitude, their effect on the flow is similar to the effect of an actual rough wall, with increasing roughness. At t_b = 500, the bedforms are still relatively small and we observe the velocity profile (dash-dotted line) to be closer to the profile of the flow over an actual rough wall (blue triangles). On the other hand, we find that when the bedforms are nearly fully developed (dashed line), the velocity profile shifts further away from the profile over a smooth wall.

At the start of the simulation, we find the logarithmic-law profile as shown in (3) to properly describe the velocity profile in the outer region when B takes on the standard value of 5.1 (Jimenez, 2004; Nikora et al., 2001). The logarithmic-law profile is given by

$$\overline{\overline{u}}_x = \frac{1}{\kappa} \ln\left(z_v^+\right) + B, \tag{3}$$

where $\kappa \approx 0.41$ is the universal von Kàrmàn constant and B is a constant that depends on the roughness of the bottom surface. As the bed evolves and the large-scale/macroscopic roughness of the sediment bed increases, B takes on smaller values of 4.1 (solid orange line) and 1.2 (solid cyan line) at t_b = 500 and 2,381, respectively (see Figure 5a). We should note here that the thickness of the layer pertaining to the logarithmic-law profile at those two instances is significantly reduced (overlap region between computed velocity profile and logarithmic-law profile), and thus, the flow has become weakly turbulent (e.g., Spalart, 1988). In fact, by inspecting the velocity profiles for the entire duration of all six simulations in Table 2, we find the coefficient B to follow a similar trend for open-channel flows with small-scale roughness (Nikuradse, 1933) as seen in Figure 5b where B is plotted as a function of the rms bed height variation in wall units, $h_{0\mathrm{rms}}^+$ ($h_{0\mathrm{rms}}^+ = h_{\mathrm{rms}}^* U_\tau^* / \nu^*$). B shows a monotonically decreasing trend with $h_{0\mathrm{rms}}^+$ starting from $h_{0\mathrm{rms}}^+ = 0$ (initial flat bed). This decreasing trend is due to the reduced flow rate over the rippled bed (as compared with the flow rate

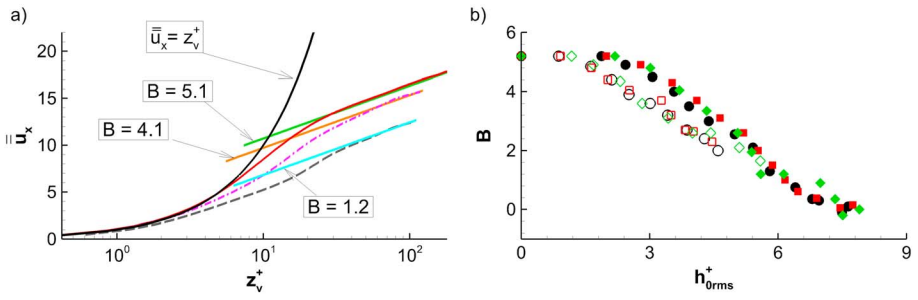

Figure 5. (a) Stream- and span-averaged x component of velocity versus vertical distance from the bed for the same instances shown in Figure 4. (b) Second coefficient in the logarithmic law of the wall versus rms bed height in wall units.

21699011, 2018, 3, Downloaded from https://agupubs.onlinelibrary.wiley.com/doi/10.1002/2017JF004399 by The University Of Texas Rio Grande Valley, Wiley Online Library on [17/02/2023]. See the Terms and Conditions (https://onlinelibrary.wiley.com/terms-and-conditions) on Wiley Online Library for rules of use; OA articles are governed by the applicable Creative Commons License

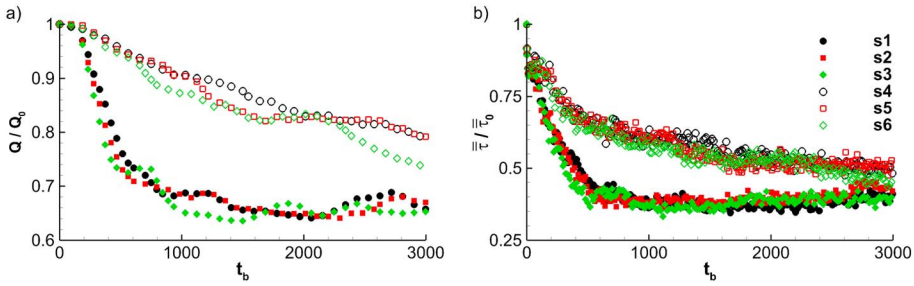

Figure 6. (a) Flow rate Q normalized by the initial flow rate Q_0 at the start of the simulation. (b) Stream- and span-averaged shear stress $\bar{\bar{\tau}}$ normalized by the stream- and span-averaged shear stress $\bar{\bar{\tau}}_0$ of the initially flattened bed at the start of the simulation.

over the initially flat bed) as a result of the emergence of bedforms coupled with the constant mean pressure gradient that is applied along the flow direction.

As the cross-sectional area of the flow varies substantially along the streamwise direction due to the presence of the rippled bed, the resistance to the flow increases, and the volumetric flow rate Q of the overlying fluid decreases over time as seen in Figure 6a. In fact, the flow rate decreases because a constant streamwise pressure gradient is maintained while the increasing bedform amplitude offers increased resistance to the flow. As mentioned previously, had the flow rate been maintained constant and the top surface allowed to evolve, then this scenario would have been different. Here the flow rate is normalized by the flow rate Q_0 over the initially flattened bed. The decrease is more rapid in the high shear cases S1–S3, and the flow rate in the presence of the mature ripples appears to settle to a new equilibrium value of about 65% of the initial value for a flat bed. As the flow rate decreases, so does the total shear stress on the bed (Figure 6b). Because of the imposed constant pressure gradient in the streamwise direction, the increase in form drag accounts for the drop in shear stress. Here again we observe the mean shear stress to reach a stationary state in the higher shear cases S1–S3. Additionally, we find the mean shear stress in the presence of the ripples to be around 40% of the initial average shear stress over a flat bed.

In the very early stages of bed evolution, when the bedforms are still very small in size, the streamlines are well aligned with the underlying topology of the sediment bed; however, as the ripples continue to develop and grow in size, the flow eventually detaches at the crest and a recirculation region forms on the lee side of the ripples (Nelson et al., 1993). For the case of fully developed flows over immobile/fixed dunes, the size of the recirculation region is primarily a function of the crest height and extends (beyond the crest) in the streamwise direction to about 4 to 6 times the crest height, measured as the elevation difference between the crest and the subsequent trough (Coleman et al., 2006; Grigoriadis et al., 2009; Kadota & Nezu, 1999; Yue et al., 2005). Here we define the size of the recirculation region (l_R) to be the farthest downstream distance from the crest (not exceeding its downstream neighbor) where the minimum span-averaged streamwise component of velocity along the z direction becomes negative. Figure 7 shows the variation of the ratio $l_R/\widehat{h}$ with respect to span-averaged crest height, measured from crest to subsequent trough for case S2 beyond $t_b = 1{,}000$ and for case S5 beyond $t_b = 2{,}500$, when the bed becomes nearly span invariant. We observe the size of the recirculation region to exhibit significant scatter, especially when the crest height is still relatively small $\widehat{h} < 0.1$. The scatter is, however, reduced for larger values of $\widehat{h}$ when the bed advances and evolves at slower speeds and bedform-bedform interactions are reduced, allowing the flow to reach a more stationary state compared to earlier times with $\widehat{h} < 0.1$. This relatively large scatter for $\widehat{h} < 0.1$ may be a result of the evolving topology, which continuously modifies the overlying flow as opposed to the fully developed flow over stationary dunes (Coleman et al., 2006, Grigoriadis et al., 2009, Kadota & Nezu, 1999, Yue et al., 2005). We

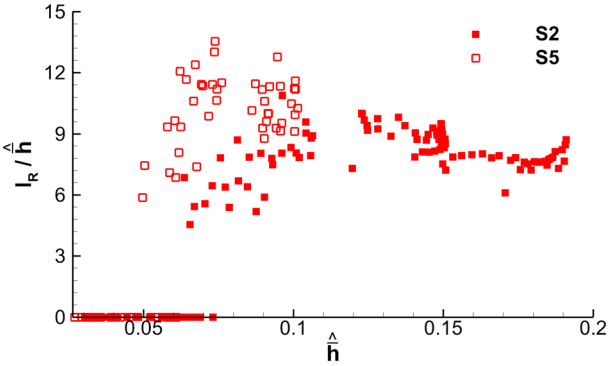

Figure 7. Streamwise extent (beyond the crest) of the recirculation region versus span-averaged crest height, measured from crest to subsequent trough. Results from S2 for $t_b > 1{,}000$ and S5 for $t_b > 2{,}500$. No recirculation is detected for values of $\widehat{h} < 0.05$.

21699011, 2018, 3, Downloaded from https://agupubs.onlinelibrary.wiley.com/doi/10.1002/2017JF004399 by The University Of Texas Rio Grande Valley, Wiley Online Library on [17/02/2023]. See the Terms and Conditions (https://onlinelibrary.wiley.com/terms-and-conditions) on Wiley Online Library for rules of use; OA articles are governed by the applicable Creative Commons License

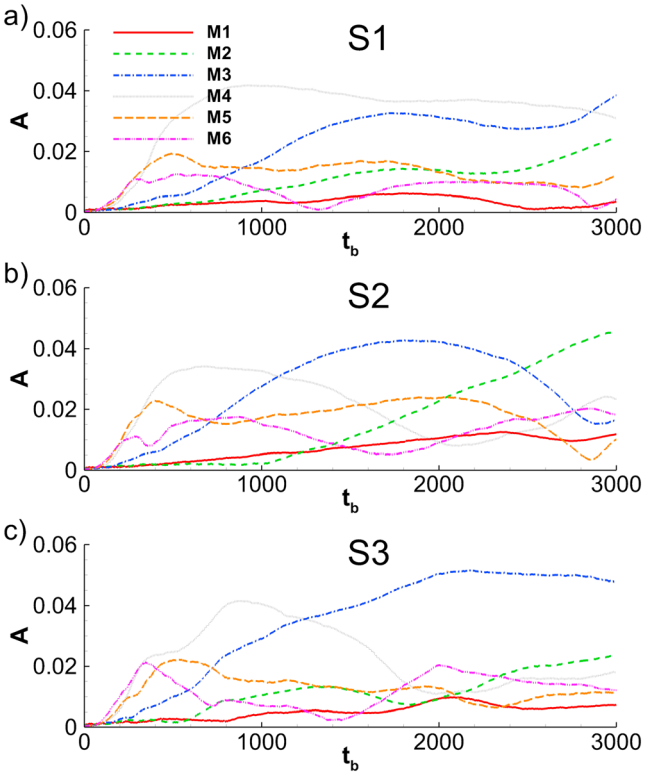

Figure 8. Temporal evolution of the amplitude of the first six Fourier modes.

should also note that the size of the recirculation region in our simulations is larger than what is reported in the simulations and experiments over fixed dunes. This may be attributed to the different bedform geometry between the aforementioned published data and our simulations, specifically that the distance between the crest and the subsequent trough in our simulations of time-evolving bedforms is larger by about 3 times than that corresponding to the fixed topology (Yue et al., 2005). Also, the Reynolds number of the present simulations is much lower (by about an order of magnitude) than those used in the experiments and simulations with fixed bedforms. Even though the bedform propagation speeds are more than 2 orders of magnitude smaller than the bulk flow velocity, we should note that the comparison with the fixed bed data may be affected by the mobility of the bed.

In addition to the aforementioned span-averaged data, we have also compute the recirculation length based on span- and time-averaged data. That is, the already span-averaged velocity field is additionally time averaged (in the frame of reference of the bed) over a time span of 25 bulk units. We observe a difference of no more than a few percent between the span-averaged data and the span-and-time-averaged data. This implies that the large scatter for relatively small bedforms in Figure 7 is not a direct result of turbulent fluctuations. In fact, as we will discuss in sections 3.3 and 4, neighboring structures could significantly impact bedform and flow dynamics and thus are likely the reason behind the relatively large scatter in Figure 7.

2.3. Temporal Evolution of Fourier Modes

Fourier analysis of the bed height variation is a natural and convenient way to quantify the wavy nature of the bed throughout the different stages of its development. It provides a quantitative method to track the apparent wavelength and amplitude of the sediment bed over time. It also provides a basis for comparing the rate of development of the bed as a function of grain diameter and shear velocity. In Figure 8, we show the time evolution of the amplitude of the first six modes for cases S1–S3. Here we perform the streamwise Fourier transform of the bed height along each spanwise y location to obtain the amplitude and phase speed of each streamwise mode and then average in the spanwise direction. In discrete form we obtain

$$F(n,y,t) = \frac{1}{N_x}\sum_{k=0}^{N_x-1} h(k\Delta x, y, t)\exp\left[-i\frac{2\pi kn}{N_x-1}\right], \tag{4}$$

$$A(n,t) = \frac{1}{N_y}\sum_{l=0}^{N_y-1}|F(n,l\Delta y,t)| \quad \& \quad c(n,t) = \frac{1}{N_y}\sum_{l=0}^{N_y-1}\frac{\lambda_n}{2\pi}\frac{\partial}{\partial t}\{\arg[F(n,l\Delta y,t)]\}\ . \tag{5}$$

Here F is the Fourier coefficient that encodes both the amplitude and phase of each of the $(N_x/2+1)$ modes (given by $n = 0, 1, 2, \ldots, N_x/2$), $i = \sqrt{-1}$, and $\lambda_n = L_x/n$ corresponds to the wavelength of the nth mode, where L_x is the size of the computational domain along the streamwise direction. This definition of amplitude and phase speed where y average is taken after x Fourier transform is appropriate as it accounts for spanwise variation in the ripple geometry. An average in the y direction followed by a Fourier transform in the x direction will be affected by spanwise incoherence of the ripples.

By tracking the spectral modes of the amplitude of bed height variation, we are able to provide a measure of the coarsening process and the spacing between bedforms. From Figure 8 we observe the rate of bedform evolution to be strongly dependent on the friction velocity of the flow. The time it takes for the amplitude of any of the modes of cases S1–S3 to grow to a value of approximately 0.02 is about 350 bulk time units, whereas for the lower shear velocity cases S4–S6, the time needed to attain the same value of amplitude is much larger at about 2,000 bulk time units. Figure 8 also provides a quantitative measure for the coarsening of the bedforms. Consider, for example, case S2, where during the early stages of bedform development for

21699011, 2018, 3, Downloaded from https://agupubs.onlinelibrary.wiley.com/doi/10.1002/2017JF004399 by The University Of Texas Rio Grande Valley, Wiley Online Library on [17/02/2023]. See the Terms and Conditions (https://onlinelibrary.wiley.com/terms-and-conditions) on Wiley Online Library for rules of use; OA articles are governed by the applicable Creative Commons License

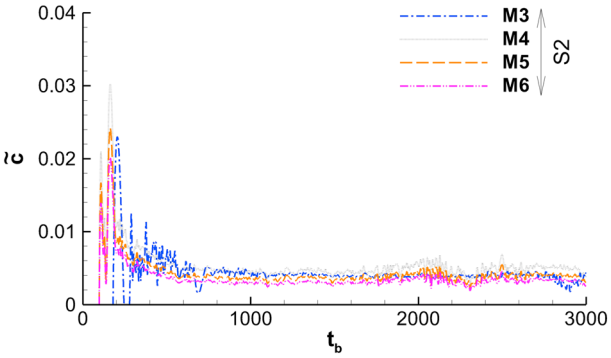

Figure 9. Temporal evolution of the phase speed $\widetilde{c}$ for modes M3 through M6 for case S2.

$100 \lesssim t_b \lesssim 200$, the higher modes ($n$ = 4–6) dominate, but with time the bedforms coarsen and progressively lower modes gain amplitude. The second mode M2 becomes the dominant mode after approximately t_b = 2,500. Additionally, for a fixed value of the shear velocity, the time it takes for the bedforms to coarsen appears to depend on the grain size, where for smaller grains, the rate of wave coarsening is higher than that for larger grains. This is consistent with the fact that for the same shear velocity, the sediment volumetric flux is larger for smaller grains and hence the rate of bedform evolution is consequently faster (Coleman & Melville, 1994).

Many studies suggest that the equilibrium wavelength of ripples scale with the grain size of the bed (e.g., Claudin & Andreotti, 2006; Flemming, 2000; Yalin, 1977). It is difficult to currently assess whether such a dependence is captured in our simulations as the bedform is still slowly evolving even after integration over a long period. We can, however, observe some indication regarding the aforementioned scaling. Keeping in mind that cases with larger shear velocities and smaller sediment size will have a larger volumetric flux of sediment, and therefore will evolve toward the equilibrium state faster than cases with smaller shear velocities and larger sediment size, now let us focus on cases S1–S3 as these will evolve faster than S4–S6. For case S3, the dominant mode beyond t_b = 1,500 is M3, corresponding to three waves within the computational domain. On the other hand, the dominant mode for case S2 beyond t_b = 2,500 is M2, corresponding to two waves. Therefore, for these two cases, the scaling is consistent with the experimental observation of longer ripple wavelengths for larger sediment size. One may argue, however, that for case S1, the dominant mode at t_b = 2,500 is M4 which does not follow the trend of S2 and S3, as one would expect the dominant mode to be at most M2. We must, however, note here that case S1 is the slowest of the three to develop, and therefore, we expect the higher modes (M3 and M4) to give way at later times in favor of M2 or even M1. We also need to keep in mind that because of the limited size of the periodic computational domain, we can only accommodate integer mode numbers. That is, while the largest possible wavelength is L_x, the next smaller possible wavelength is $L_x/2$, with no in-between values permitted. The spectral counts of wavelengths do not necessarily capture the much smaller bedforms, but they are consistent with the manual counts of dominant bedforms. For example, for case S2, we clearly observe, beyond t_b = 1,500, two dominant bedforms along with two much smaller bedforms.

The phase speed c(n, t) in (5) provides a good measure of the speed of propagation of a specific mode and indirectly the speed of the bed as a whole. Figure 9 shows the temporal evolution of the phase speed $\widetilde{c}$ for modes, M3 through M6, for case S2. Here $\widetilde{c}$ is the phase speed normalized by the bulk velocity, $\widetilde{c} = c\, U_\tau^*/U_b^*$. At early times when the bed is still evolving, we observe $\widetilde{c}(n,t)$ to be chaotic. In fact, when the amplitude of the modes is still very small, say $A(n,t) < 7 \times 10^{-3}$, the modes are very susceptible to fluctuations imposed by the turbulent bed shear stress. Once $A(n,t)$ grows large enough, we observe the fluctuations in $\widetilde{c}$ to decrease significantly. Consider mode M3 in Figure 8b whose amplitude only surpasses a value of 7×10^{-3} around t_b = 500, which corresponds approximately to the time when the fluctuations of $\widetilde{c}$ for mode M3 in Figure 10 are significantly reduced. We observe $\widetilde{c}$ to be nearly independent of the mode number and to be indicative of the velocity of the bed as a whole.

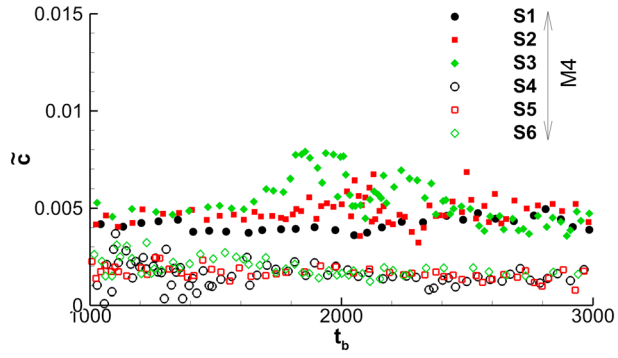

Figure 10. Temporal evolution of the phase speed $\widetilde{c}$ for the fourth mode M4 from the six cases, S1 through S6.

Once the bedforms are fully developed, the time evolution of the bed as a whole strongly resembles the evolution of a single spectral mode. In Figure 10, we plot the time evolution of the fourth mode M4 for the six cases, S1 through S6 beyond t_b = 1,000, when the fluctuations have sufficiently diminished. We observe the phase speed for the relatively high U_τ^* cases S1–S3 to be about 3 times larger than the low U_τ^* cases S4–S6. On the other hand, we observe $\widetilde{c}$ to be marginally affected by the grain size. The phase speed of the other modes is also qualitatively similar to that shown in Figure 10. Therefore, it appears that the phase speed of the different modes substantially varies

21699011, 2018, 3, Downloaded from https://agupubs.onlinelibrary.wiley.com/doi/10.1002/2017JF004399 by The University Of Texas Rio Grande Valley, Wiley Online Library on [17/02/2023]. See the Terms and Conditions (https://onlinelibrary.wiley.com/terms-and-conditions) on Wiley Online Library for rules of use; OA articles are governed by the applicable Creative Commons License

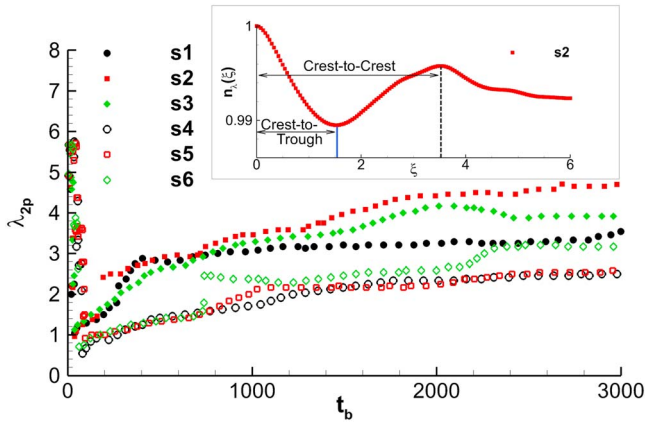

Figure 11. Dominant bed height wavelength λ_{2p} versus time. Inset: two-point correlation function versus separation ξ showing the dominant crest-to-trough and crest-to-crest separation at t_b = 1,220 for case S2.

over time as a result of the nonlinear interaction between the different modes in terms of the bedform interactions.

2.4. Two-Point Correlation

A two-point correlation analysis of the bed provides a single effective value for bed wavelength and bed velocity as a function of time. These values may then be contrasted with those for the individual modes obtained from the Fourier analysis. In Figure 11, we present the dominant wavelength λ_{2p} and the bed velocity $\widetilde{c}_{2p}$, which has been normalized by the flow bulk velocity. Here and in the remainder of the paper, the subscript 2*p* corresponds to a value obtained using the two-point correlation. The two-point correlation function $n_\lambda(\xi, t)$ of the bed elevation is defined as follows:

$$n_\lambda(\xi,t) = \frac{\int_0^{L_y}\int_0^{L_x} h(x,y,t)h(x+\xi,y,t)\mathrm{d}x\mathrm{d}y}{\int_0^{L_y}\int_0^{L_x} h(x,y,t)h(x,y,t)\mathrm{d}x\mathrm{d}y}. \quad (6)$$

The dominant wavelength λ_{2p} is defined as the value of ξ at which the two-point correlation function attains its first peak. Here we discount the peak corresponding to ξ = 0. A representative plot of the two-point correlation function versus separation ξ is shown in Figure 11 as an inset at t_b = 1,220 for case S2. The correlation function n_λ is normalized and thus has a maximum of unity. Because of periodicity in the streamwise direction, we only need to consider the separation ξ for half the domain length, that is, $0 < \xi < L_x/2$ as n_λ is symmetric about $\xi = L_x/2 = 6$. The distance between ξ = 0 and the first and only minimum (in this case) denoted by the vertical solid blue line at $\xi \approx 1.5$ corresponds to the dominant crest-to-subsequent-trough separation. On the other hand, the distance between ξ = 0 and the first and only maximum (for this specific case) denoted by the vertical dashed black line at $\xi \approx 3.5$, which is usually the highest peak of n_λ over the entire domain (excluding ξ = 0), represents the dominant wavelength λ_{2p}, that is, the dominant crest-to-crest separation. For the time considered in the inset (t_b = 1,220), the correlation function only exhibits a single minimum as well as a single maximum over the range $0 < \xi < L_x/2$. While this might be the case for relatively long time (i.e., $t_b \gtrsim$ 1,200), the correlation function n_λ displays multiple maxima and minima at earlier times, whose amplitudes usually decrease with increasing values of separation ξ. These multiple maxima and minima are indicative of the presence of multiple bedforms whose separation is inferred from the distance between these maxima and minima. We should note that if all the bedforms are perfectly periodic in the streamwise direction, then the amplitude of all the maxima (and minima) as well as their crest-to-crest (and crest-to-trough) separations would be identical.

At the very early stages of bed development, the bedform is very chaotic due to the dominant influence of the overlying turbulent flow, which results in large fluctuations in the value of λ_{2p} (Figure 11 for $t_b \lesssim 50$). However, once the chevron features begin to emerge, we are able to obtain meaningful values of λ_{2p}, where for all six cases considered, we see an increasing trend due to wave coarsening. Here as well, we observe the effect of the applied shear stress and the grain size on the development of the bed. During early times, for $t_b \lesssim 600$, we observe λ_{2p} for cases S1–S3 to increase faster by about a factor of 2 compared to cases S4–S6. We should note here that this faster rate does not explicitly depend on the bedload flux model we use. A smaller flux of sediment restricts the bed to a slower evolution rate and hence the slower rate observed in Figure 11 for cases S4–S6. Additionally, at these early times, we observe the grain size to only marginally affect the value of λ_{2p} as well as its rate of increase. At later times, $t_b \gtrsim$ 1,500 for S1–S3 and $t_b \gtrsim$ 2,200 for S4–S6, we observe the effect of the grain size on λ_{2p} to become important. For case S1, because of the larger grain size, λ_{2p} increases at a slower rate compared to cases S2 and S3. If the present simulations are to be representative of field observations and laboratory experiments, then we would expect λ_{2p} from case S1 to eventually be the larger of the three after the bed is given enough time to evolve. As mentioned earlier in section 2.3, we observe an indication of this trend with cases S2 and S3 where λ_{2p} for case S2 is larger than that for case S3. As for the lower shear stress cases, S4–S6, they require much longer integration times to display the increasing wavelength scaling with grain size for equilibrium ripples. By $t_b \approx$ 2,200, we observe

21699011, 2018, 3, Downloaded from https://agupubs.onlinelibrary.wiley.com/doi/10.1002/2017JF004399 by The University Of Texas Rio Grande Valley, Wiley Online Library on [17/02/2023]. See the Terms and Conditions (https://onlinelibrary.wiley.com/terms-and-conditions) on Wiley Online Library for rules of use; OA articles are governed by the applicable Creative Commons License

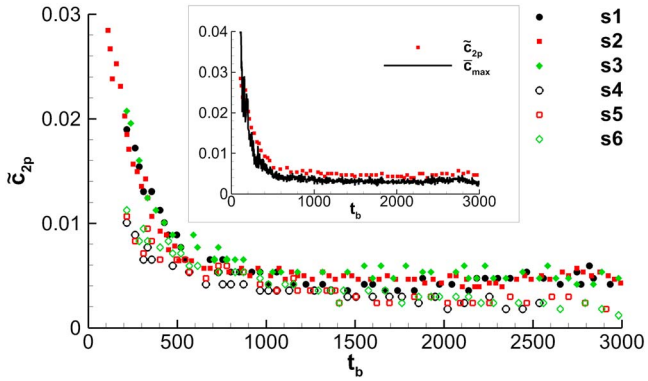

Figure 12. Temporal evolution of $\widetilde{c}_{2p}$, the bed velocity normalized by the bulk velocity U_b^*. Inset: temporal evolution of $\widetilde{c}_{2p}$ and $\widetilde{c}_{\max}$ for case S2.

λ_{2p} for case S6 to peel off from the other two slowly evolving cases and approach λ_{2p} for case S3. In all the cases, the slow increase in λ_{2p} is clearly indicative of the slow coarsening trend exhibited by the ripples.

As the bedform coarsens the mean wavelength of the ripples and the ripple height accordingly increase. This process of growth is limited by the height of the ripple, either by altering the turbulence production process or through interaction with the free surface, or by reaching a critical velocity at the crest (Flemming, 2000). Here we discuss near-equilibrium states, which remain stable for very long time, and consider properties of this near-equilibrium state, such as wavelength of the ripples and their dependence on grain size and flow depth.

For evaluating the effective phase speed of the bedform, we define the normalized space-time correlation as follows:

$$n_c(\chi,\varsigma,t)=\frac{\int_0^{L_y}\int_0^{L_x}h(x,y,t)h(x+\chi,y,t+\varsigma)\mathrm{d}x\mathrm{d}y}{\int_0^{L_y}\int_0^{L_x}h(x,y,t)h(x,y,t)\mathrm{d}x\mathrm{d}y}. \tag{7}$$

For a fixed value of $\varsigma = 3\times10^{-2}$ we compute the space-time correlation and obtain the value of χ that maximizes n_c. The nondimensional bed velocity is then obtained as $c_{2p}=\chi_{\max}/\varsigma$. In Figure 12, we show the time evolution of $\widetilde{c}_{2p}=c_{2p}U_\tau^*/U_b^*$ for the six cases S1 through S6. This value of ς corresponds to a $\Delta t_b = 0.47$. Space-time correlation obtained for other values of ς remains qualitatively similar and the conclusions to be drawn are robust and insensitive to the above choice of ς.

A decreasing trend for the bed velocity over time as in the phase speed plot in Figure 9 is observed. Here again, we note the marginal effect the grain size has on the celerity of the waves with very little differences observed among cases S1–S3 and S4–S6, respectively. On the contrary, we observe the bed shear stress, imposed by the overlying flow, to dictate the speed at which the bed evolves during all stages of bedform evolution. Additionally, at late times $t_b \gtrsim 2{,}000$, the value of the bed velocity from cases S1–S3 is approximately 3 times that from cases S4–S6.

Finite amplitude ripples advance at a velocity c obtained from mass conservation on the lee side (Charru et al., 2016; Coleman & Melville, 1994) as

$$c=\frac{q}{\widehat{h}}, \tag{8}$$

where q is the volumetric sediment flux per unit width at the crest and the ripple height $\widehat{h}$ is measured from the crest to the subsequent trough. In the inset of Figure 12, we show the velocity $\widetilde{c}_{\max}$ of the largest span-averaged ripple alongside $\widetilde{c}_{2p}$ for case S2. Here $\widetilde{c}_{\max}$ is defined as follows:

$$\widetilde{c}_{\max}=\frac{U_\tau^*\,\overline{q}_{\max}}{U_b^*\,\widehat{\overline{h}}_{\max}}, \tag{9}$$

where $\widehat{\overline{h}}_{\max}$ is the maximum height of the span-averaged bed, measured from crest to subsequent trough and $\overline{q}_{\max}$ is the span-averaged sediment flux per unit width at the crest of the largest ripple. From the inset of Figure 12, we find $\widetilde{c}_{\max}$ to follow the same trend and to have a value that is close to but smaller than $\widetilde{c}_{2p}$. Recall that $\widetilde{c}_{\max}$ is based on the largest ripple and consequently is expected to be slower than the average velocity of the bed.

3. Ripple Self-Similarity

3.1. Shape Self-Similarity

Yalin (1977) argues that ripple development may be divided into two phases. During the first relatively short-lived phase, ripples grow in both size and steepness. A growth in steepness indicates that the rate of growth

21699011, 2018, 3, Downloaded from https://agupubs.onlinelibrary.wiley.com/doi/10.1002/2017JF004399 by The University Of Texas Rio Grande Valley, Wiley Online Library on [17/02/2023]. See the Terms and Conditions (https://onlinelibrary.wiley.com/terms-and-conditions) on Wiley Online Library for rules of use; OA articles are governed by the applicable Creative Commons License

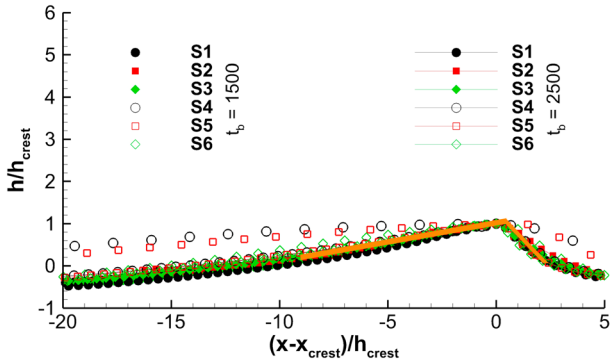

Figure 13. Cross-sectional shape of the largest ripple in the center plane (y = 2) for all S* cases in Table 2 at t_b = 1,500 (symbols) and t_b = 2,500 (symbols + lines). The ripple height and length have been scaled by the respective crest height (h_{crest}). Additionally, all the ripples have been translated along the x axis for comparison. The orange segments provide an estimate of the slope at the stoss and lee sides of the rippels, which approximately correspond to an angle of 5° and 30°, respectively.

of the height of the ripple is faster than the rate of growth of the ripple's length. On the other hand, during the second phase, ripples mainly grow in their size, that is, in both height and length, maintaining a geometrically nearly similar shape. That is the ripple's height and length grow at comparable rates. In the following section, we find the bed evolution to match Yalin's (1977) hypothesis for the presence of two phases during ripple growth. First, recall that mature ripples are characterized by a gentle slope on the stoss side and a steeper slope on their lee side equivalent to the angle of repose. Since the sediment bed is initially flat, it follows that the ripple must initially steepen and as the ripple grows the slope on the lee side plateaus toward the angle of repose. Additionally, once the slope on the lee side approaches the angle of repose, we observe the ripples to grow in size, while maintaining a nearly self-similar profile.

Once the bed becomes nearly span invariant, a vertical slice of the bed may be used to quantify the shape of the bed in the entire domain. Figure 13 shows a ripple from the cross section of the bed in the $y = L_y/2$ center plane for all S* cases in Table 2. Two times are considered, namely, t_b = 1,500 and t_b = 2,500. In each case, the ripple is translated along the streamwise direction by a distance that corresponds to the location of the crest (x_{crest}). In order to align the ripple crests in the plot, the ripple height for each case is also scaled both in the streamwise and vertical directions by the respective crest height (h_{crest}). Except for cases S4 and S5 at t_b = 1,500, the ripples demonstrate a nearly self-similar triangular-like profile with a gentle slope on the stoss side and a steeper lee side dictated by the angle of repose (α_R = 30°). The thick solid orange line overlaying the stoss side of the ripples provides an estimate for the slope that corresponds approximately to a 6° angle. Alternatively, the thick orange line on the lee side has a slope that corresponds to the imposed angle of repose. As can be clearly seen in Figure 13, cases S4 and S5 at the early time of t_b = 1,500 deviate from the self-similar profile. The slopes on both sides of the crest for these cases are smaller than those observed for the self-similar profile. Recall that these two cases correspond to the lower bed shear stress value and larger grain diameter (see Table 2). Therefore, on average, the volumetric flux of sediment is the lowest for these two cases, and consequently, the ripples are slow to develop. Thus, these two profiles have not reached their self-similar state by t_b = 1,500.

On the other hand, for the same 2 cases, S4 and S5 at the later time of t_b = 2,500, the ripples demonstrate the aforementioned triangular self-similar shape. By this time, the vertical drop from the crest to the subsequent trough of the tallest ripple is 0.08 and 0.09 for S4 and S5, respectively, whereas at t_b = 1,500, the vertical drops were approximately 2 times smaller at 0.05 and 0.04 for S4 and S5, respectively. In fact, for all the ripples in Figure 13 that exhibit the self-similar profile, the vertical drop from the crest to the subsequent trough was above 0.08. This suggests that there is a minimum vertical drop above which the cross-sectional shape of the ripple approaches the self-similar profile. Additionally, the self-similar profile displayed in Figure 13 may only be reached once the slope on the lee side corresponds to the angle of repose. Furthermore, by inspecting over 250 ripples at various stages of evolution for the six S* cases, we find this minimum or threshold vertical drop to be around 0.07, which is equivalent to about 4, 7, and 20 grains for S1–S3, respectively.

We have considered the cross-sectional shape of the different ripples that are present in a bed at a specific instant during bed development (e.g., the five ripples seen in Figure 3k in Paper 1) and the cross-sectional shape of the same ripple as it evolves over time (e.g., the ripples that are tracked in Figure 3 (Paper 1) from frame k to frame l). We have also considered the variation in the shape of the ripple from one bed to the other where the flow conditions are kept unchanged, but sediment properties, such as sediment size, are modified (S1 versus S2 versus S3). Alternatively, for different flow conditions but with identical sediment properties (S1 versus S4). In all these cases, once the height of the ripple grows large enough such that the lee side corresponds to the sediment angle of repose, the cross-sectional shape of the ripple is observed to conform to the triangular self-similar shape. This self-similar shape appears to be independent of grain size and flow conditions (Simons et al., 1965). The stoss side of the self-similar profile has an inclination of about 6°, which is consistent with previous studies using DNS (Kidanemariam & Uhlmann, 2017) and

21699011, 2018, 3, Downloaded from https://agupubs.onlinelibrary.wiley.com/doi/10.1002/2017JF004399 by The University Of Texas Rio Grande Valley, Wiley Online Library on [17/02/2023]. See the Terms and Conditions (https://onlinelibrary.wiley.com/terms-and-conditions) on Wiley Online Library for rules of use; OA articles are governed by the applicable Creative Commons License

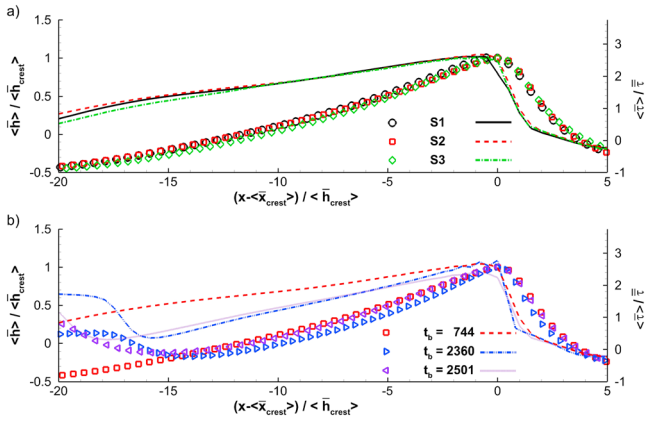

Figure 14. (a) The symbols correspond to the span-averaged cross-sectional shape of a span invariant, isolated ripple at t_b = 744 from S1 to S3 scaled by the span-averaged crest height. The lines correspond to the span- and time-averaged shear stress for each ripple scaled by the instantaneous span- and stream-averaged shear stress. (b) Same as Figure 14a but for the same ripple from S2 at different times. The presence of an upstream neighbor modifies the shear stress on the stoss side and eventually leads the cross-sectional shape to a deviate from the self-similar profile.

experiments in the field (Fourrière et al., 2010), whereas the slope at the lee side is dictated by the angle of repose. In fact, a necessary condition for self-similarity is the development of an avalanche slip-face (corresponding to the angle of repose) on the bedform's lee side. We will elaborate on the conditions that cause developing ripples to deviate from self-similarity in the next section.

3.2. Bed Shear Stress Self-Similarity

Owing to the fact that the Exner equation is used to evolve the sediment bed, it follows that for the ripple cross section to attain and maintain a self-similar shape, the sediment flux and consequently the bed shear stress must also be self-similar. With that in mind, we have considered in Figure 14a the cross-sectional shape (denoted by symbols) of three self-similar ripples from cases S1–S3 along with the associated bed shear stress profiles (denoted by lines) at t_b = 744. Unlike the cross-sectional shape of ripples, which evolves on a much longer time scale compared to the overlying flow field, the bed shear stress is inherently turbulent with substantial local and instantaneous fluctuations mirroring the passing of near-bed intense turbulent eddies. Therefore, instead of showing an instantaneous cross section of a ripple with its turbulent bed shear stress profile, we make use of the nearly span-invariant bedforms to average in the spanwise direction. Additionally, because of the separate time scales over which the bed and the flow evolve, we average the shear stress within a sufficiently small time window of seven bulk time units, during which the ripple translates by less than one grid cell. The time over which the averaging is performed needs to be large enough to filter out the local and instantaneous fluctuations but small enough such that the flow sees a stationary ripple. Time averaging, which is denoted in the figure by the angular brackets, is only needed for the shear stress profiles; however, to remain consistent, we also average the bed height variation $\overline{h}$ over the same time period. Here again, the bed height variation is normalized by the span- and time-averaged crest height, $\overline{h}_{\text{crest}}$. Similarly, we scale the span- and time-averaged shear stress $\overline{\tau}(x,t)$ by the instantaneous bed-averaged shear stress $\overline{\overline{\tau}}(t)$. Similar to Figure 13, we observe the averaged ripple cross sections to exhibit the same self-similar triangular profile. Additionally, the profiles of the shear stress are also found to be nearly self-similar with an analogous triangular shape displaying a gentle rise on the stoss side of the ripple, followed by a steep drop in the region approximately one ripple height around the crest of the ripple, which is further followed by a slow drop in the shear stress for the remainder of the lee side. The time and location of the ripples in the figure are chosen such that they are sufficiently far from upstream and downstream neighbors so that they may be considered locally isolated in the sense that the overlying flow field is weakly or negligibly influenced by the presence of neighboring structures. Neighboring structures, as we will shortly see, can significantly alter the overlying flow field and consequently the bed shear stress profiles. We should also note the presence of the positive phase shift between the shear stress and cross-sectional shape of the ripple at the crest. The maximum shear stress does not occur at the crest but slightly upstream toward the end of the stoss side. This phase shift is primarily responsible for the growth of the ripple. While sediment inertia, in the context of coarse sediments, has been used as a possible explanation for the presence of such a phase shift in laboratory experiments (Parker, 1975), here we observe the phase shift to come out naturally from the hydrodynamic nature of the flow.

To further illustrate how bedform-bedform interactions cause a self-similar ripple to deviate from self-similarity, we show in Figure 14b the same cross-sectional shape of the self-similar ripple from S2 at three time instances, namely, t_b = 744, 2,350, and 2,501. The first time instance (t_b = 744) is the same as that shown in frame a and corresponds to the self-similar profile. The subsequent instances are chosen at a time when a smaller upstream neighbor (blue symbols) approaches the stoss side of the ripple in question. As can be seen from the figure, the upstream neighbor is smaller and thus able to catch up to the self-similar ripple. In addition to the obvious deformation this smaller upstream ripple causes to the cross-sectional shape of the self-similar ripple, it also significantly modifies the shear stress over the entire stoss side of the ripple. For example, the shear stress at $(x-\overline{x}_{\text{crest}})/\overline{h}_{\text{crest}} = -15$ is reduced by approximately 3 to 5 times by t_b = 2,350 and 2,501,

21699011, 2018, 3, Downloaded from https://agupubs.onlinelibrary.wiley.com/doi/10.1002/2017JF004399 by The University Of Texas Rio Grande Valley, Wiley Online Library on [17/02/2023]. See the Terms and Conditions (https://onlinelibrary.wiley.com/terms-and-conditions) on Wiley Online Library for rules of use; OA articles are governed by the applicable Creative Commons License

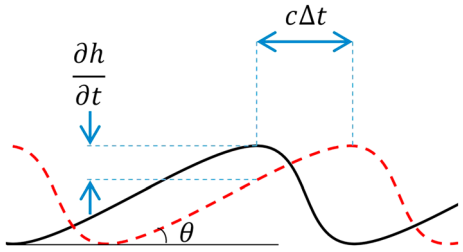

Figure 15. Schematic for a self-similar ripple at time t (solid black line) and $t + \Delta t$ (dashed red line) undergoing pure translational motion, with no growth or decay, at a velocity c.

respectively, compared to the self-similar profile at t_b = 744. While the deviation from self-similarity in terms of the cross-sectional shape needs time to develop, the shear stress profiles are rapidly modified on the turbulent flow time scale. These new modified shear stress profiles now act to modify the bedload fluxes on the stoss side eventually leading to a departure of the ripple from its self-similar shape. These examples highlight the approach to self-similarity of a ripple and departure from self-similarity when acted upon by an upstream neighbor.

3.3. Characterization of the Self-Similar State

One of the characteristics of ripples is their asymmetrical triangular shape in which the slope on the stoss side corresponds to a few degrees, while the slope on the lee side is much steeper and is usually dictated and corresponds to the angle of repose of the sediment grains. Here we provide a very simple and crude analysis to estimate the slope of the stoss side from the self-similar shear stress profiles. In Figure 15, we show a schematic of a two-dimensional self-similar ripple undergoing pure translational motion. The solid black line corresponds to the profile of the ripple at time t, while the red dashed line corresponds to the profile at a later time $t + \Delta t$ where the ripple has translated along the streamwise direction by a distance $c\,\Delta t$. To simplify matters, we consider the ripple speed c to be a temporally and spatially independent constant; additionally, the ripple does not grow or decay but rather keeps the exact same cross-sectional shape and simply translates downstream. Since we are interested in extracting the bed slope on the stoss side, we compute the height variation as follows:

$$\frac{\Delta h}{\Delta t} = c\tan\theta, \tag{10}$$

where θ is the inclination on the stoss side of the ripple. It follows from the Exner equation (as $\Delta t \to 0$) that if we neglect the diffusion term, the inclination of the stoss side may be expressed as follows:

$$\theta = -\tan^{-1}\left(\frac{1}{c\varphi}\frac{\mathrm{d}q}{\mathrm{d}x}\right), \tag{11}$$

where φ corresponds to the volume fraction of the sediment bed and q is the volumetric flux of sediment due to bedload. By considering the cross section of a self-similar ripple from S3 at t_b = 2,009 in Figure 16 along with the span- and time-averaged (over the same small period of seven bulk time units as in Figure 14) x component of the volumetric flux of sediment q_x, we extract the spatial variation $(\mathrm{d}\bar{q}_x/\mathrm{d}x)$ on a portion of the stoss side bounded by the vertical thin dashed lines such that it is sufficiently far from the crest and the base of the stoss side. By substituting for the values on the right-hand side in (11), we find $\theta \approx 5°$, which is consistent with the actual computed inclination of the stoss side of a self-similar ripple of $\theta \approx 6°$ in Figure 13 as well as previously published data (Kidanemariam & Uhlmann, 2017). Equation (11) also indicates that for a ripple to retain its self-similarity as it evolves, the ripple speed and the spatial variation of the bedload flux must vary proportionally with one another.

Once the ripples attain a self-similar profile, their height and wavelengths become strongly interdependent in such a way that as the bedforms coarsen, their height, measured from crest to subsequent trough, must also proportionally increase. For each ripple that has grown to its self-similar shape we define its wavelength $\widehat{\lambda}$ as the streamwise distance between its upstream and downstream troughs. Correspondingly, the ripple height $\widehat{h}$ is defined as the vertical distance from the crest to the downstream trough. In Figure 17, we plot $\widehat{\lambda}$ versus $\widehat{h}$ only for self-similar ripples from cases S1 to S6. We observe the wavelength to height ratio of the ripples in the self-similar phase to be approximately 25, consistent with previously reported data from DNS of Kidanemariam and Uhlmann (2017) as well as laboratory experiments and field studies (Flemming, 2000). The dashed line in Figure 17 corresponds to an aspect ratio of 20, which has been reported by Andreotti and Claudin (2013). They argue that when the ripple aspect ratio approximately reaches this value, the ripple amplitude saturates and the slope on the lee side of the ripple corresponds to the angle of repose.

The spectral and two-point correlation analyses showed that the speed of the bedform decreased over time, while the mean wavelength and height of the ripples increased. Here we will directly quantify the correlation

21699011, 2018, 3, Downloaded from https://agupubs.onlinelibrary.wiley.com/doi/10.1002/2017JF004399 by The University Of Texas Rio Grande Valley, Wiley Online Library on [17/02/2023]. See the Terms and Conditions (https://onlinelibrary.wiley.com/terms-and-conditions) on Wiley Online Library for rules of use; OA articles are governed by the applicable Creative Commons License

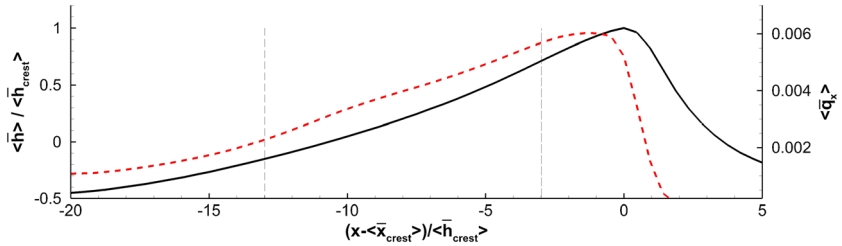

Figure 16. Cross-sectional shape (black solid line) of a span- and time-averaged self-similar ripple from S3 at t_b = 2,009 along with the span- and time-averaged streamwise component of bedload flux (red dashed line). The *x* axis and the bed height variation are normalized by the crest height.

between ripple height and ripple velocity and compare the simulation results against previous laboratory experiments. Coleman and Melville (1994) conducted a series of laboratory experiments with sand particles with mean grain size of 200 μm and 820 μm. They observed the speed of the rippled bedform to be inversely proportional to the ripple height and proposed the following empirical fit:

$$\widehat{c}\left(\widehat{h}^*/d_p^* - 3.5\right)^{1.3} = 40, \tag{12}$$

where they defined the nondimensional ripple speed $\widehat{c}$ as follows:

$$\widehat{c} = \frac{c^*}{\left(u_\tau^* - u_{\tau,\mathrm{cr}}^*\right)\left(\Theta - \Theta_{\mathrm{cr}}\right)}, \tag{13}$$

where $u_{\tau,\mathrm{cr}}^*$ represents the critical shear velocity. Venditti (2003) conducted similar experiments in a flume with sand particles of mean grain size 500 μm. In Figure 18, we show a plot of $\widehat{c}$ versus $\widehat{h}/d_p$ from the present simulations S1 through S6 as well as from the laboratory experiments of Coleman and Melville (1994) and Venditti (2003). The data points for our simulations were only obtained for ripples in the self-similar phase. To obtain the ripple speed $\widehat{c}$ from the simulations, we span average the bed, after it has become nearly span invariant, and track the largest ripples that exhibit a self-similar profile. For these ripples, we compute the temporal evolution of the streamwise speed of the crest, as well as the vertical drop between the crest and the subsequent trough. We observe good agreement between the simulation data and the empirical fit of Coleman and Melville (1994) for values of $\widehat{h}/d_p > 20$ and reasonable agreement for smaller values of $\widehat{h}/d_p$, where the present data lie below the empirical fit. We note, however, that the values that do not fall exactly on the proposed fit are still within the experimental data scatter reported in Coleman and Melville (1994) and Venditti (2003). Additionally, we find our data to correspond more closely to the following empirical fit:

$$\widehat{c}\,\frac{\widehat{h}}{d_p}\ln\left(\frac{\widehat{h}}{d_p}\right) = 45. \tag{14}$$

From Figures 17 and 18, it can be observed that the streamwise size (or wavelength) of a ripple and its speed are primarily influenced by the ripple height. However, these plots also suggest that additional factors besides the crest height could also affect the size and the speed of the ripples. The large scatter in Figure 18 and also the scatter seen in the wavelength versus wave height plot indicate imperfect correlation between these quantities. Indeed, the scatter in Coleman and Melville (1994) data can at times exceed a factor of 4, which seems too large to simply attribute to experimental uncertainty. Similarly, the scatter in our simulation results is also not due to numerical noise. We observe the presence and proximity of neighboring bedforms downstream and upstream to play a key role in dictating the wavelength and speed of every bedform. It is clear that for a ripple, the approach of an upstream or downstream ripple close to it will result in a decrease of its wavelength, defined as the distance between the upstream and downstream troughs. It was demonstrated in Figure 14 that the effect of an upstream neighbor can be significant in terms of local bedload transport of sediment on the stoss side. It appears that the

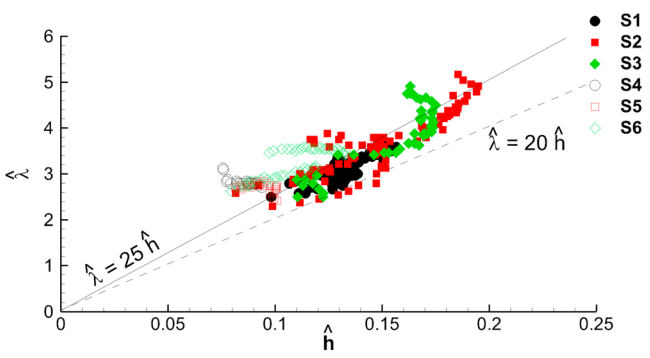

Figure 17. Wavelength versus wave height for self-similar ripples from cases S1 to S6.

21699011, 2018, 3, Downloaded from https://agupubs.onlinelibrary.wiley.com/doi/10.1002/2017JF004399 by The University Of Texas Rio Grande Valley, Wiley Online Library on [17/02/2023]. See the Terms and Conditions (https://onlinelibrary.wiley.com/terms-and-conditions) on Wiley Online Library for rules of use; OA articles are governed by the applicable Creative Commons License

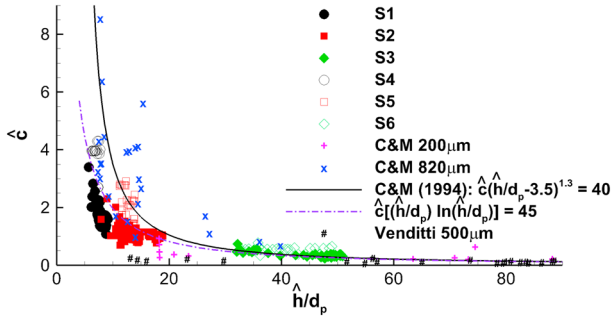

Figure 18. Ripple speed versus ripple height for self-similar ripples for cases S1 through S6. Present data are compared with the empirical fit (black solid line) and laboratory measurements ({+, x} for {200, 820}μm sand particle, respectively) of Coleman and Melville (1994) and laboratory measurement (#) of Venditti (2003). The dash-dotted line $\hat{c}\frac{\hat{h}}{d_p}\ln\left(\frac{\hat{h}}{d_p}\right) = 45$ provides a better fit to the present data.

proximity of neighboring structures through such interactions also leads to substantial variation in the ripple speed. In fact, interactions between neighboring ripples are the main cause of ripple growth and decay, and in general ripple dynamics. These aspects will be further addressed in the following section.

4. Bedform Coarsening

Bedform coalescence or wave coarsening occurs when two separate bedforms interact or come together to produce a single discrete structure (Raudkivi & Witte, 1990). Because the speed of bedforms is inversely proportional to their height, bedform coarsening is generally initiated by an upstream smaller structure approaching a larger downstream structure. Consequently, for coarsening to occur, one of the two interacting structures must grow, while the other must diminish and gradually disappear (Coleman & Melville, 1994). The first possibility is for the upstream bedform to ride up the stoss side and merge with the larger downstream structure, a mechanism that is identical to the merging sequence involving defects described in Paper 1. However, unlike defects, here merging occurs across the entire span of the interacting bedforms, that is, for the entire nearly span-invariant ripple. The second possibility is for the upstream structure to grow by starving the downstream neighbor. This mechanism is yet again identical to bedform repulsion (described in Paper 1) but occurs across the entire span of the interacting bedforms. The first of the two possibilities, merging, usually occur when the upstream neighbor is too small to starve the larger downstream structure. This is usually a result of a limited sediment supply caused by a noneroding flow on the base of the stoss side of the upstream neighbor. The second possibility, which consists of the upstream structure starving its downstream neighbor, occurred more often in the simulations and was also found to be a predominant (over the first) coarsening feature in the experiments of Coleman and Melville (1994). Additionally, when this starving process occurs, the starving/diminishing bedform could be either absorbed by the upstream growing neighbor, or alternatively, could temporarily escape and merge with a larger downstream structure. But this second scenario is the same as first possibility where a weak ripple merges with its downstream neighbor, but in this case this merging process is driven by the upstream neighbor of the weak ripple. In other words, a third ripple that is not involved in the merging process is driving the interaction, which can be considered as remote interaction.

In the remainder of this section, we consider the ripples from case S2 as we track the coarsening process that progressively leads to fewer and larger bedforms. Figure 19 shows a spanwise-averaged side view of the bed with isocontours of the streamwise component of velocity $\overline{u}_x$ at $t_b = 515$. We identify five ripples, in which the crests and corresponding troughs are marked sequentially by C_n and T_n (with n going from 1 to 5), respectively. The height of the first three ripples are large enough to induce substantial flow separation on their lee side. At this time, the bedforms span the entire width of the domain and have become nearly spanwise-invariant/two-dimensional, except for ripple 5, which from a top view of the bed appears to be rather sinuous. In fact, the degree of two dimensionality may be inferred from the overall shape of the ripple as well as the slopes on the stoss and lee sides. For example, the slope on the lee side of ripple 5 is almost equivalent to that on its stoss side, and the ripple's cross-sectional shape resembles more a symmetric isosceles triangle than the characteristic asymmetric triangular shape. This indicates that the crest line C_5 is not straight but rather sinuous so that the spanwise-averaged slope is nearly identical downstream and upstream of the crest.

The coarsening sequence of case S2 is investigated by tracking the subsequent interactions among the five bedforms beyond the time shown in Figure 19. In Figure 20, we show a time series of the spanwise-averaged bed revealing a remote interaction between C_4 and C_5. The interaction is illustrated through four time instances. From the cross-sectional view in Figure 20a, we observe C_4 to be smaller than C_5 and thus approaches the latter. As discussed earlier, when the separation between the bedforms decreases beyond a certain threshold, there are two possible outcomes for which either C_4 or C_5 survives after the interaction. In this particular situation, C_4 is sufficiently far away from C_3 such that it is able to grow and starve its downstream neighbor C_5 as shown in Figure 20b. Recall that the domain is periodic in the streamwise direction

21699011, 2018, 3, Downloaded from https://agupubs.onlinelibrary.wiley.com/doi/10.1002/2017JF004399 by The University Of Texas Rio Grande Valley, Wiley Online Library on [17/02/2023]. See the Terms and Conditions (https://onlinelibrary.wiley.com/terms-and-conditions) on Wiley Online Library for rules of use; OA articles are governed by the applicable Creative Commons License

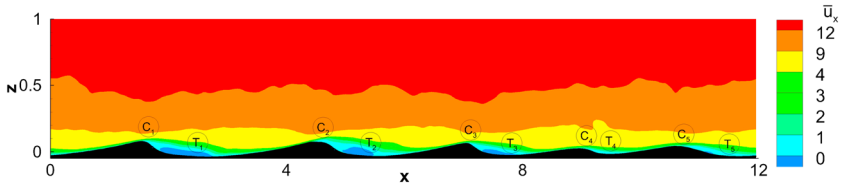

Figure 19. Span-averaged bed and streamwise component of velocity for case S2 at $t_b = 515$ when the bed has become nearly span invariant. The bed consists of five ripples, and troughs are marked as C∗ and T∗, respectively. Note that because of periodicity, T_5 is also the trough upstream of C_1.

such that ripple C_4 is still upstream of C_5 in Figure 20b. The continuously diminishing crest C_5 is pushed away toward C_1, and as can be seen by the elongated stoss side of ripple 1 in frame d (relative to frame c), C_5 merges with its downstream neighbor C_1. In fact, by looking at videos of the simulations for other cases, we find that the diminishing ripple (C_5 in the present case) merges with its downstream neighbor (C_1 in the present case) when the latter is sufficiently close. On the other hand, if the downstream neighbor (C_1 in the present case) is not close enough, the diminishing ripple is unable to escape in time and becomes part of the trough of the upstream neighbor (C_4 in the present case). Such a scenario is later observed in the coalescing remote interaction between C_4 and C_1 (not shown here), in which C_4 starves and gobbles up the latter.

4.1. Ripple Statistics

We can analyze ripple statistics by identifying each ripple by its crest and its downstream trough, where by definition, each crest is separated from its upstream and downstream neighbors by a trough. Due to its self-similar shape, each crest will be characterized by its span-averaged height $\overline{h}_c$ and its span-averaged streamwise location $\overline{x}_c$. Correspondingly, each trough will be denoted by its depth (negative height $-\overline{h}_t$ below the mean bed elevation) and its streamwise location $\overline{x}_t$ (see Figure 20a). Time histories of $\overline{x}_c, \overline{h}_c, \overline{x}_t$, and $\overline{h}_t$ for all the crests and troughs of case S2 are shown in Figure 21 frames a, c, d, and f, respectively. Also shown in the figure are $d\overline{x}_c/dt$ and $d\overline{x}_t/dt$, which correspond to the span-averaged velocity of the crest and the trough, respectively. Whenever one of the lines in each frame is discontinued, a coarsening/coalescing interaction takes place in which a peak disappears, with the corresponding disappearance of either its upstream or downstream trough, depending on the nature of the interaction. The first crest and trough to disappear are those corresponding to C_5 and T_5, respectively. The other interacting bedform in this coarsening process is ripple 4. Let us examine the speeds and elevation of those two bedforms during the interaction. From Figure 21b, we observe the speed of C_4 to decay while that of C_5 to rise, where the rates of decay and rise

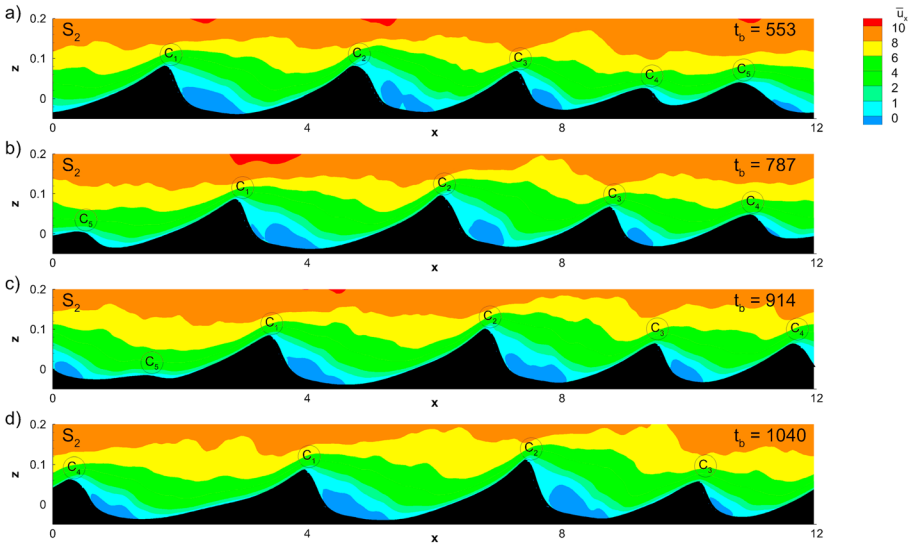

Figure 20. Time series of the spanwise-averaged bed and streamwise component of velocity from case S2 showing wave coarsening through remote interaction. The diminished ripple C_5 in frame c goes on to merge with the downstream ripple C_1.

21699011, 2018, 3, Downloaded from https://agupubs.onlinelibrary.wiley.com/doi/10.1002/2017JF004399 by The University Of Texas Rio Grande Valley, Wiley Online Library on [17/02/2023]. See the Terms and Conditions (https://onlinelibrary.wiley.com/terms-and-conditions) on Wiley Online Library for rules of use; OA articles are governed by the applicable Creative Commons License

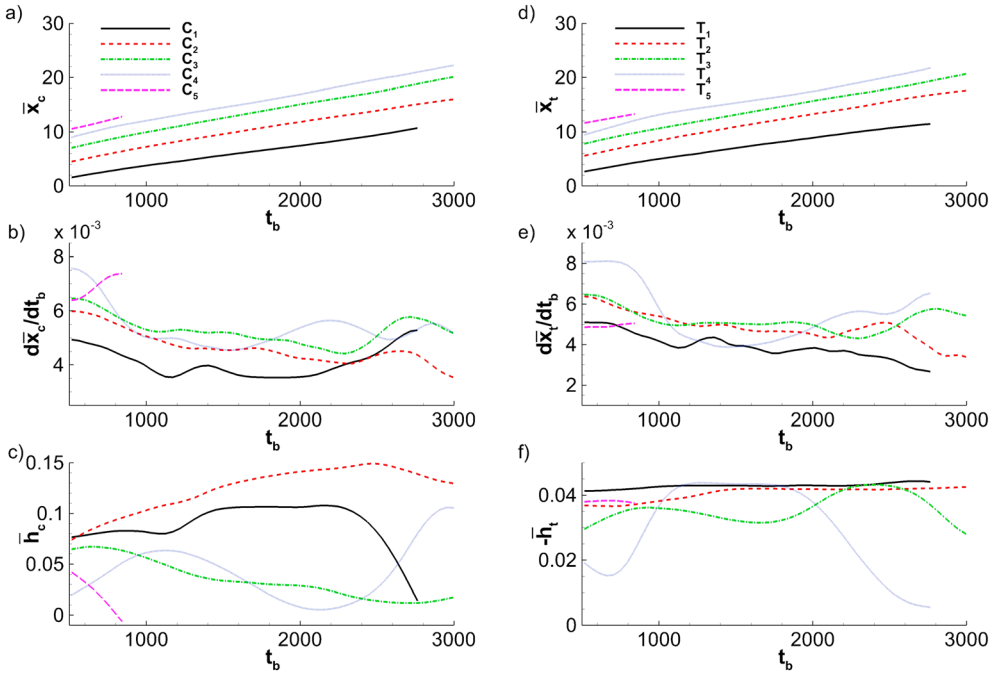

Figure 21. Temporal evolution of spanwise-averaged quantities from case S2 of (a) crest position, (b) crest velocity, (c) above mean crest elevation, (d) trough position, (e) trough velocity, and (f) below mean trough depth.

are roughly similar. Additionally, we observe the crest elevation of C_4 in Figure 21c to rise, while that of the diminishing ripple C_5 decreases, again at roughly the same rate. Moreover, we observe the trough T_4 to rise, toward the initial mean elevation, in accordance with ripple 4 acting to starve and absorb its downstream neighbor C_5. Similarly, in a subsequent interaction around t_b = 2,700 between C_1 and C_4, we observe the same dynamics with regard to ripple speed and elevation of the interacting bedforms. The speed of the upstream neighbor C_4 momentarily decreases, while its crest elevation increases and its trough depth approaches the initial mean bed height. On the other hand, the speed of the diminishing downstream neighbor C_1 increases while its crest height drops. In both these instances, a finite ripple vanishes and consequently the number of bedforms in the domain is reduced.

To assess the effect of the coarsening interaction on the dynamics of ripples, specifically on the relation between height and speed, we evaluated the speed of the ripples involved in a coarsening interaction based on the empirical relation in (14). We found a relatively large discrepancy between the computed values from (14) and the observed values in the simulations. For example, at t_b = 787, which corresponds to the side view of Figure 20b where ripples 4 and 5 are in the process of coalescing into a single ripple, we find the crest speeds of C_4 and C_5 as predicted by (14) to be about 3 and 5 times larger than the actual speeds in Figure 21b, respectively. On the other hand, for a ripple not currently involved in any coalescing interaction such as C_2, we find the speed of the crest predicted by (14) to be within 10% of the actual speed in Figure 21b. This large discrepancy between the predicted and actual velocities for interacting bedforms is likely to contribute to the relatively large scatter observed in Figure 18. Therefore, while the crest height remains the principal factor that dictates the ripple speed, neighboring structures may temporarily and significantly influence the rate of propagation of ripples as they come into close proximity with the bedform in question. In addition to altering the ripple speeds, neighboring structures also strongly influence the growth/decay rates of adjacent bedforms.

Finally, we note that the time needed to complete the coalescing interaction is much longer (up to 10 times) than that needed to complete the defect-related interactions during the early times of bed evolution (discussed in Paper 1) (Perillo et al., 2014). This is consistent with the fact that during the later stages of bed evolution, the bedforms are larger in size (i.e., move relatively slow) and are more spaced out (i.e., must cover larger distances to interact with a downstream or upstream neighbor). This is contrary to the bed at early times, which is characterized by relatively small, closely spaced structures. It is important to note that in

21699011, 2018, 3, Downloaded from https://agupubs.onlinelibrary.wiley.com/doi/10.1002/2017JF004399 by The University Of Texas Rio Grande Valley, Wiley Online Library on [17/02/2023]. See the Terms and Conditions (https://onlinelibrary.wiley.com/terms-and-conditions) on Wiley Online Library for rules of use; OA articles are governed by the applicable Creative Commons License

field observations (Ewing & Kocurek, 2010), certain interactions involving very large-scale bedforms can take up to decades to complete, while other interactions involving small ripples can occur in seconds or minutes.

5. Discussion

An important observation of the present work is that the cross-sectional outline of an isolated mature ripple takes on a nearly self-similar shape. However, the shape of a ripple can deviate from the self-similar profile when it interacts or becomes substantially influenced by a neighboring ripple or bedform. At times, as the crest height of a ripple decays in amplitude due to bedform-bedform interaction, for example, we find its cross-sectional profile to progressively deviate from self-similarity. This supports the observation that ripples maintain a self-similar shape provided that their height is larger than the aforementioned threshold height of 0.07 nondimensional units. In other words, ripples as they grow in size take on a self-similar shape when their size exceeds a threshold, and ripples as they decay in size, lose their self-similar shape when their size falls below a threshold value. If flow conditions and sediment availability are maintained, then bedforms will only decay when acted upon by upstream neighbors. That is a mature ripple that is sufficiently far from an upstream neighbor will remain self-similar until it is "preyed" upon by an upstream neighbor or experiences a change in flow conditions or sediment availability.

Bedform self-similarity (or lack-of) is also closely related to bedform dynamics, specifically the bedform propagation velocity as well as its rates of growth and decay. As bedforms interact, and thus deviate from self-similarity, we observe sharp variations in their speeds and growth/decay rates. Therefore, when measurements of celerity versus size of bedforms are recorded, it is important to note whether the bedform in question is sufficiently isolated so that the measurements are not influenced by nearby structures. Such practice could reduce the amount of scatter, and thus reduce the uncertainty, in these measurements.

There is a clear distinct behavior between the two sets of simulations in Table 2, namely, S1–S3 and S4–S6. A natural question that arises is whether this is a physical result or some consequence of the modeling employed in the present study, specifically the modified Meyer-Peter and Müller (1948) bedload relation of Wong and Parker (2006). The only difference between the two sets of simulations is that in the latter (S4–S6) the friction velocity has been decreased, while the flow depth has been accordingly increased so as to maintain the same shear Reynolds number Re_τ. The two series, however, exhibit different bedform propagation velocities, different wavelengths, etc.

It is observed that the nondimensional bedform propagation velocity (scaled with the shear velocity) decreases with decreasing shear velocity between sets S1–S3 and S4–S6. Let us consider a limiting case for which the flow depth is very large and the bed shear velocity is very small so as to maintain a constant Re_τ. The critical shear velocity necessary for incipient motion is now much larger than the bed shear velocity, and consequently, there should be no sediment motion, or in other words, the bedform propagation velocity should be 0. Starting from this limiting case, let us gradually increase the bed shear velocity (while simultaneously decreasing the flow depth). There will come a point where the bed shear velocity would exceed the critical shear velocity necessary for incipient motion, and the sediments would be set in motion.

The nondimensional parameter that is responsible for this distinct behavior is the Shields number Θ or, more specifically, the ratio of the Shields number to the critical Shields number necessary for incipient motion (Θ/Θ_{cr}). This dependence on Θ/Θ_{cr} is captured in the MPM (and consequently in the Wong and Parker modified MPM) formulation and is responsible for the distinct behavior between the two sets of data. This can also be explained in terms of the three length scales: the channel height, wall unit (ν/u_*) and the particle diameter. In both sets, the ratio of channel height to wall unit remains the same, since Re_τ is a constant. Thus, as the channel got taller the near-wall eddies also correspondingly became bigger. However, if the particle size is kept the same, with decreasing U_τ^* the ability of the turbulent flow to move the particles changes.

6. Conclusions

Coupled bed-flow DNS presented in Part 1 describe the early stages of pattern formation by ripples in an open-channel flow analyzed using a highly resolved flow field. In the present paper (Part 2), we compare the simulations to published experimental data and quantitatively analyze the bed using spectral analysis

21699011, 2018, 3, Downloaded from https://agupubs.onlinelibrary.wiley.com/doi/10.1002/2017JF004399 by The University Of Texas Rio Grande Valley, Wiley Online Library on [17/02/2023]. See the Terms and Conditions (https://onlinelibrary.wiley.com/terms-and-conditions) on Wiley Online Library for rules of use; OA articles are governed by the applicable Creative Commons License

and two-point correlations. The effect of the mobile rippled bed on the flow structure as well as turbulence was investigated locally (at specific streamwise locations) and over the entire computational domain. We showed that developing ripples attain a self-similar profile in both the shape and the corresponding bed shear stress profile. We further demonstrated the importance of neighboring structures, especially upstream neighbors, on bedform dynamics in terms of the growth, decay, and speed of ripples. Finally, we examined the defect-free interactions in the later stages of bed evolution, which primarily lead to wave coarsening.

Analysis of turbulence statistics indicates no qualitative difference in velocity fluctuations or the Reynolds stress profiles from a rippled and completely flat bed. However, velocity fluctuations increased near the bed at the expense of the mean flow as the ripples grew. Applying a logarithmic-law velocity profile for the span-averaged streamwise component of velocity in the far field yields an intercept that follows a trend similar to open-channel flows with small-scale roughness. Accurate calculation of the velocity fluctuations and Reynolds stresses requires the application of a coordinate frame that it is normal to the bed in the near-bed region and turns to the vertical direction sufficiently far away.

A quantitative analysis of the emerging bedforms revealed a -3.75 power decay for large wave numbers in the spectra for developing ripples. Similar values were obtained in previous DNS of Kidanemariam and Uhlmann (2017). The decay is, however, faster than the -3 decay reported in the earlier experiments of Hino (1968), Jain and Kennedy (1974), and Nikora et al. (1997). The shear Reynolds number in the present study and from the numerical simulations of Kidanemariam and Uhlmann (2017) were more than an order of magnitude smaller than those calculated from the aforementioned experiments suggesting a possible Reynolds number dependence for bedform spectra.

Analyses from Fourier decomposition and two-point correlations of ripple properties such as crest height, wavelengths, and celerity indicated that the ripples increase in height and coarsen with time, with the speed of the ripple being inversely proportional to its crest height. Additionally, as the ripple height, measured as the elevation difference between the crest and the subsequent trough, increases beyond a threshold value, we observe the ripples to approach a nearly self-similar triangular-like shape characterized by a gentle stoss side of about 6° and a steeper lee side dictated by the angle of repose. Within this self-similar phase, we find the relationship between the ripple speed and height to agree with the empirical relation proposed by Coleman and Melville (1996). The self-similarity in the ripple shape is accompanied by an analogous self-similar triangular-like bed shear stress profile. There is, however, a positive phase shift between the streamwise location of the crest and the location of the maximum of the shear stress profile, for which the latter occurs slightly upstream of the crest. Through a simple and very crude analysis of the self-similar shear stress profile on the stoss side of the ripple, we are able to recover the computed gentle slope on the stoss side suggesting that the shape and bed shear stress profiles are strongly coupled.

The experimental data of Coleman and Melville (1996) exhibit considerable scatter around their aforementioned empirical fit. This scatter appears too large to be simply attributed to experimental uncertainty but is likely a result of bedform-bedform interactions. Based on the present simulations, we find the relationship between the speed and the size of isolated mature ripples to follow the empirical fit of Coleman and Melville (1996); however, when neighboring ripples get within close proximity of the ripple in question (for which a relationship between the ripple speed and size is sought), we find the actual speed to significantly deviate from the speed predicted by the proposed fit by up to five times.

Of the six simulations considered, those with higher bed shear velocities (cases S1–S3) evolved faster than those with larger flow depths but smaller bed shear velocities (casesS4 – S6) owing to their larger volumetric flux of sediment. While bed shear velocity is the principal factor dictating the velocity of the bed for the entire duration of the simulations, we find that grain size has only a marginal effect.

Cases with higher bed shear velocities coarsen at a faster rate compared to cases with lower bed shear velocities. On the other hand, at later times toward the end of the simulations, there is an indication that ripple wavelength scales with the grain diameter, with smaller sediment exhibiting smaller wavelengths. The current work could be improved by considering the following two factors. First, ripples did not reach an equilibrium state by the end of the simulations even after long time integration of 3,000 bulk time units because the purpose of these runs was to examine ripple initiation and early time evolution (Paper 1) as well as ripple dynamics in the developing stage before reaching equilibrium. Second, these simulations lack essential

21699011, 2018, 3, Downloaded from https://agupubs.onlinelibrary.wiley.com/doi/10.1002/2017JF004399 by The University Of Texas Rio Grande Valley, Wiley Online Library on [17/02/2023]. See the Terms and Conditions (https://onlinelibrary.wiley.com/terms-and-conditions) on Wiley Online Library for rules of use; OA articles are governed by the applicable Creative Commons License

physics, such as the saltation mechanism, for capping crest growth and may therefore be inappropriate for studying the equilibrium stage of ripple evolution but are suitable for investigating developing ripples during the period in when bedload constitutes the dominant mode of sediment transport.

Acknowledgments
We are grateful to ExxonMobil Upstream Research Company for providing support through grant number EM09296. Numerical data presented herein will be available in the Sediment Experimentalists Network (SEN) Knowledge Base (http://www.sedexp.net).

References

Andreotti, B., & Claudin, P. (2013). Aeolian and subaqueous bedforms in shear flows. *Philosophical Transactions of the Royal Society A*, *371*(2004), 20120364.

Andrle, R. (1996). The west coast of Britain: Statistical self-similarity vs. characteristic scales in the landscape. *Earth Surface Processes and Landforms*, *21*(10), 955–962. https://doi.org/10.1002/(SICI)1096-9837(199610)21:10%3C955::AID-ESP639%3E3.0.CO;2-Y

Ashley, G. M. (1990). Classification of large-scale subaqueous bedforms: A new look at an old problem-SEPM bedforms and bedding structures. *Journal of Sedimentary Research*, *60*(1).

Balachandar, R., Polatel, C., Hyun, B. S., Yu, K., Lin, C. L., Yue, W., & Patel, V. C. (2003). LDV, PIV and LES investigation of flow over a fixed dune. In *Sedimentation and sediment transport* (pp. 171–178). Netherlands: Springer.

Barabási, A. L., & Stanley, H. E. (1995). *Fractal concepts in surface growth*. Cambridge, UK: Cambridge University Press. https://doi.org/10.1017/CBO9780511599798

Bennett, S. J., & Best, J. L. (1995). Mean flow and turbulence structure over fixed, two-dimensional dunes: Implications for sediment transport and bedform stability. *Sedimentology*, *42*(3), 491–513. https://doi.org/10.1111/j.1365-3091.1995.tb00386.x

Best, J. (1992). On the entrainment of sediment and initiation of bed defects: Insights from recent developments within turbulent boundary layer research. *Sedimentology*, *39*(5), 797–811. https://doi.org/10.1111/j.1365-3091.1992.tb02154.x

Best, J., & Kostaschuk, R. (2002). An experimental study of turbulent flow over a low-angle dune. *Journal of Geophysical Research*, *107*(C9), 3135. https://doi.org/10.1029/2000JC000294

Chan-Braun, C., García-Villalba, M., & Uhlmann, M. (2011). Force and torque acting on particles in a transitionally rough open-channel flow. *Journal of Fluid Mechanics*, *684*, 441–474. https://doi.org/10.1017/jfm.2011.311

Charru, F., Andreotti, B., & Claudin, P. (2013). Sand ripples and dunes. *Annual Review of Fluid Mechanics*, *45*(1), 469–493. https://doi.org/10.1146/annurev-fluid-011212-140806

Charru, F., Bouteloup, J., Bonometti, T., & Lacaze, L. (2016). Sediment transport and bedforms: A numerical study of two-phase viscous shear flow. *Meccanica*, *51*(12), 3055–3065. https://doi.org/10.1007/s11012-016-0553-5

Charru, F., & Mouilleron-Arnould, H. (2002). Instability of a bed of particles sheared by a viscous flow. *Journal of Fluid Mechanics*, *452*, 303–323.

Claudin, P., & Andreotti, B. (2006). A scaling law for aeolian dunes on Mars, Venus, Earth, and for subaqueous ripples. *Earth and Planetary Science Letters*, *252*(1-2), 30–44. https://doi.org/10.1016/j.epsl.2006.09.004

Coco, G., & Murray, A. B. (2007). Patterns in the sand: From forcing templates to self-organization. *Geomorphology*, *91*(3-4), 271–290. https://doi.org/10.1016/j.geomorph.2007.04.023

Coleman, S. E., & Melville, B. W. (1994). Bed-form development. *Journal of Hydraulic Engineering*, *120*(5), 544–560. https://doi.org/10.1061/(ASCE)0733-9429(1994)120:5(544)

Coleman, S. E., & Melville, B. W. (1996). Initiation of bed forms on a flat sand bed. *Journal of Hydraulic Engineering*, *122*(6), 301–310. https://doi.org/10.1061/(ASCE)0733-9429(1996)122:6(301)

Coleman, S. E., & Nikora, V. I. (2011). Fluvial dunes: Initiation, characterization, flow structure. *Earth Surface Processes and Landforms*, *36*(1), 39–57. https://doi.org/10.1002/esp.2096

Coleman, S. E., Nikora, V. I., McLean, S. R., Clunie, T. M., Schlicke, T., & Melville, B. W. (2006). Equilibrium hydrodynamics concept for developing dunes. *Physics of Fluids*, *18*(10), 105104. https://doi.org/10.1063/1.2358332

Einstein, H. A., & Barbarossa, N. (1952). River channel roughness. *Transactions of the American Society of Civil Engineers*, *117*, 1121–1146.

Engelund, F. (1977). Hydraulic resistance for flow over dunes. Inst. Hydrodyn. and hydraulic Engrg. Tech. Univ. Denmark, Proc. Rep. 44 (pp. 19–20).

Ewing, R. C., & Kocurek, G. A. (2010). Aeolian dune interactions and dune-field pattern formation: White Sands Dune Field, New Mexico. *Sedimentology*, *57*(5), 1199–1219.

Fedele, J. J., & García, M. H. (2001). Alluvial roughness in streams with dunes: A boundary-layer approach. In *River, coastal and estuarine morphodynamics* (pp. 37–60). Berlin Heidelberg: Springer.

Flemming, B. W. (2000). The role of grain size, water depth and flow velocity as scaling factors controlling the size of subaqueous dunes. In *Marine sandwave dynamics, International Workshop* (pp. 23–24). Lille, France.

Fourrière, A., Claudin, P., & Andreotti, B. (2010). Bedforms in a turbulent stream: Formation of ripples by primary linear instability and of dunes by nonlinear pattern coarsening. *Journal of Fluid Mechanics*, *649*, 287–328. https://doi.org/10.1017/S0022112009993466

Franklin, E. D. M., & Charru, F. (2009). Morphology and displacement of dunes in a closed-conduit flow. *Powder Technology*, *190*(1-2), 247–251. https://doi.org/10.1016/j.powtec.2008.04.065

Grigoriadis, D. G. E., Balaras, E., & Dimas, A. A. (2009). Large-eddy simulations of unidirectional water flow over dunes. *Journal of Geophysical Research*, *114*, F02022. https://doi.org/10.1029/2008JF001014

Gyr, A., & Schmid, A. (1997). Turbulent flows over smooth erodible sand beds in flumes. *Journal of Hydraulic Research*, *35*(4), 525–544. https://doi.org/10.1080/00221689709498409

Hanmaiahgari, P. R., & Balachandar, R. (2016). Turbulence characteristics of open channel flow over non-equilibrium 3-D mobile dunes. *Sādhanā*, *41*(9), 1019–1037.

Hino, M. (1968). Equilibrium-range spectra of sand waves formed by flowing water. *Journal of Fluid Mechanics*, *34*(03), 565–573. https://doi.org/10.1017/S0022112068002089

Howard, A. D. (2007). Simulating the development of Martian highland landscapes through the interaction of impact cratering, fluvial erosion, and variable hydrologic forcing. *Geomorphology*, *91*(3-4), 332–363. https://doi.org/10.1016/j.geomorph.2007.04.017

Jain, S. C., & Kennedy, J. F. (1974). The spectral evolution of sedimentary bed forms. *Journal of Fluid Mechanics*, *63*(02), 301–314. https://doi.org/10.1017/S0022112074001157

Jerolmack, D. J., & Mohrig, D. (2005). A unified model for subaqueous bed form dynamics. *Water Resources Research*, *41*, W12421. https://doi.org/10.1029/2005WR004329

Jimenez, J. (2004). Turbulent flows over rough walls. *Annual Review of Fluid Mechanics*, *36*(1), 173–196. https://doi.org/10.1146/annurev.fluid.36.050802.122103

21699011, 2018, 3, Downloaded from https://agupubs.onlinelibrary.wiley.com/doi/10.1002/2017JF004399 by The University Of Texas Rio Grande Valley, Wiley Online Library on [17/02/2023]. See the Terms and Conditions (https://onlinelibrary.wiley.com/terms-and-conditions) on Wiley Online Library for rules of use; OA articles are governed by the applicable Creative Commons License

Kadota, A., & Nezu, I. (1999). Three-dimensional structure of space-time correlation on coherent vortices generated behind dune crest. *Journal of Hydraulic Research*, *37*(1), 59–80. https://doi.org/10.1080/00221689909498532

Kidanemariam, A. G., & Uhlmann, M. (2014). Direct numerical simulation of pattern formation in subaqueous sediment. *Journal of Fluid Mechanics*, *750*, R2. https://doi.org/10.1017/jfm.2014.284

Kidanemariam, A. G., & Uhlmann, M. (2017). Formation of sediment patterns in channel flow: Minimal unstable systems and their temporal evolution. *Journal of Fluid Mechanics*, *818*, 716–743.

Kocurek, G., Ewing, R. C., & Mohrig, D. (2010). How do bedform patterns arise? New views on the role of bedform interactions within a set of boundary conditions. *Earth Surface Processes and Landforms*, *35*(1), 51–63. https://doi.org/10.1002/esp.1913

Maddux, T. B., Nelson, J. M., & McLean, S. R. (2003). Turbulent flow over three-dimensional dunes: 1. Free surface and flow response. *Journal of Geophysical Research*, *108*(F1), 6009. https://doi.org/10.1029/2003JF000017

McLean, S. R., Nelson, J. M., & Wolfe, S. R. (1994). Turbulence structure over two-dimensional bed forms: Implications for sediment transport. *Journal of Geophysical Research*, *99*, 12,729–12,747. https://doi.org/10.1029/94JC00571

Meyer-Peter, E., & Müller, R. (1948). Formulas for bed-load transport. In *Proceedings of 2nd meeting of the International Association for Hydraulic Structures Research, Oskar Eklunds Boktryckeri* (pp. 39–64). Stockholm, Sweden.

Nelson, J. M., McLean, S. R., & Wolfe, S. R. (1993). Mean flow and turbulence fields over two-dimensional bed forms. *Water Resources Research*, *29*, 3935–3953. https://doi.org/10.1029/93WR01932

Nelson, J. M., & Smith, J. D. (1989). Mechanics of flow over ripples and dunes. *Journal of Geophysical Research*, *94*, 8146–8162. https://doi.org/10.1029/JC094iC06p08146

Nikora, V., Goring, D., McEwan, I., & Griffiths, G. (2001). Spatially averaged open-channel flow over rough bed. *Journal of Hydraulic Engineering*, *127*(2), 123–133. https://doi.org/10.1061/(ASCE)0733-9429(2001)127:2(123)

Nikora, V. I., Sukhodolov, A. N., & Rowinski, P. M. (1997). Statistical sand wave dynamics in one-directional water flows. *Journal of Fluid Mechanics*, *351*, 17–39.

Nikuradse, J. (1933). Gesetzmäßigkeiten der turbulenten Strömung in glatten Rohren (Nachtrag). *Forschung auf dem Gebiet des Ingenieurwesens A*, *4*(1), 44–44. https://doi.org/10.1007/BF02716946

Omidyeganeh, M., & Piomelli, U. (2013). Large-eddy simulation of three-dimensional dunes in a steady, unidirectional flow. Part 1. Turbulence statistics. *Journal of Fluid Mechanics*, *721*, 454.

Ouriemi, M., Aussillous, P., & Guazzelli, E. (2009a). Sediment dynamics. Part 1. Bed-load transport by laminar shearing flows. *Journal of Fluid Mechanics*, *636*, 295–319. https://doi.org/10.1017/S0022112009007915

Ouriemi, M., Aussillous, P., & Guazzelli, E. (2009b). Sediment dynamics. Part 2. Dune formation in pipe flow. *Journal of Fluid Mechanics*, *636*, 321–336. https://doi.org/10.1017/S0022112009007927

Parker, G. (1975). Sediment inertia as cause of river antidunes. *Journal of the Hydraulics Division*, *101*(2), 211–221.

Pelletier, J. D. (2013). Deviations from self-similarity in barchan form and flux: The case of the Salton Sea dunes, California. *Journal of Geophysical Research: Earth Surface*, *118*, 2406–2420. https://doi.org/10.1002/2013JF002867

Perillo, M. M., Best, J. L., Yokokawa, M., Sekiguchi, T., Takagawa, T., & Garcia, M. H. (2014). A unified model for bedform development and equilibrium under unidirectional, oscillatory and combined-flows. *Sedimentology*, *61*(7), 2063–2085. https://doi.org/10.1111/sed.12129

Raudkivi, A. J., & Witte, H. H. (1990). Development of bed features. *Journal of Hydraulic Engineering*, *116*(9), 1063–1079. https://doi.org/10.1061/(ASCE)0733-9429(1990)116:9(1063)

Ribberink, J. S., & Al-Salem, A. A. (1994). Sediment transport in oscillatory boundary layers in cases of rippled beds and sheet flow. *Journal of Geophysical Research*, *99*, 12,707–12,727. https://doi.org/10.1029/94JC00380

Schindler, R. J., & Robert, A. (2005). Flow and turbulence structure across the ripple–dune transition: An experiment under mobile bed conditions. *Sedimentology*, *52*(3), 627–649. https://doi.org/10.1111/j.1365-3091.2005.00706.x

Simons, D. B., Richardson, E. V., & Nordin, C. F. (1965). Sedimentary structures generated by flow in alluvial channels. In G. V. Middleton (Ed.), *Primary sedimentary structures and their hydrodynamic interpretation, Society of Economic Paleontologists and Mineralogists* (pp. 34–52). Tulsa, OK.

Spalart, P. R. (1988). Direct simulation of a turbulent boundary layer up to $R\theta = 1410$. *Journal of Fluid Mechanics*, *187*(1), 61–98. https://doi.org/10.1017/S0022112088000345

Swanson, T., Mohrig, D., Kocurek, G., & Liang, M. (2016). A surface model for Aeolian dune topography. *Mathematical Geosciences*, 1–21.

Venditti, J. G. (2003). Initiation and development of sand dunes in river channels (Doctoral dissertation). University of British Columbia.

Venditti, J. G., & Bennett, S. J. (2000). Spectral analysis of turbulent flow and suspended sediment transport over fixed dunes. *Journal of Geophysical Research*, *105*, 22,035–22,047. https://doi.org/10.1029/2000JC900094

Werner, B. T. (1995). Eolian dunes: Computer simulations and attractor interpretation. *Geology*, *23*(12), 1107–1110. https://doi.org/10.1130/0091-7613(1995)023%3C1107:EDCSAA%3E2.3.CO;2

Werner, B. T. (1999). Complexity in natural landform patterns. *Science*, *284*(5411), 102–104. https://doi.org/10.1126/science.284.5411.102

Werner, B. T. (2003). Modeling landforms as self-organized, hierarchical dynamical systems. In *Prediction in geomorphology* (pp. 133–150). Washington, DC: American Geophysical Union.

Wong, M., & Parker, G. (2006). Reanalysis and correction of bed-load relation of Meyer-Peter and Müller using their own database. *Journal of Hydraulic Engineering*, *132*(11), 1159–1168. https://doi.org/10.1061/(ASCE)0733-9429(2006)132:11(1159)

Yalin, M. S. (1977). *Mechanics of sediment transport*. Tarrytown, New York: Pergamon.

Yue, W., Lin, C. L., & Patel, V. C. (2005). Coherent structures in open-channel flows over a fixed dune. *Journal of Fluids Engineering*, *127*(5), 858–864. https://doi.org/10.1115/1.1988345

Zedler, E. A., & Street, R. L. (2001). Large-eddy simulation of sediment transport: Currents over ripples. *Journal of Hydraulic Engineering*, *127*(6), 444–452. https://doi.org/10.1061/(ASCE)0733-9429(2001)127:6(444)

Zgheib, N., Fedele, J. J., Hoyal, D. C. J. D., Perillo, M. M., & Balachandar, S. (2018). Direct numerical simulation of transverse ripples: 1. Pattern initiation and bedform interactions. *Journal of Geophysical Research: Earth Surface*, *123*. https://doi.org/10.1002/2017JF004398

21699011, 2018, 3, Downloaded from https://agupubs.onlinelibrary.wiley.com/doi/10.1002/2017JF004399 by The University Of Texas Rio Grande Valley, Wiley Online Library on [17/02/2023]. See the Terms and Conditions (https://onlinelibrary.wiley.com/terms-and-conditions) on Wiley Online Library for rules of use; OA articles are governed by the applicable Creative Commons License